

# Self-gravitational Magnetohydrodynamics with Adaptive Mesh Refinement for Protostellar Collapse

Tomoaki MATSUMOTO

*Faculty of Humanity and Environment, Hosei University, Fujimi, Chiyoda-ku, Tokyo 102-8160, Japan  
matsu@i.hosei.ac.jp*

(Received 2006 September 5; accepted 2007 June 25)

## Abstract

A new numerical code, called SFUMATO, for solving self-gravitational magnetohydrodynamics (MHD) problems using adaptive mesh refinement (AMR) is presented. A block-structured grid is adopted as the grid of the AMR hierarchy. The total variation diminishing (TVD) cell-centered scheme is adopted as the MHD solver, with hyperbolic cleaning of the divergence error of the magnetic field also implemented. The MHD solver exhibits a second-order accuracy in convergence tests of linearized MHD waves. The self-gravity is solved using a multigrid method composed of (1) a full multigrid (FMG)-cycle on the AMR hierarchical grids, (2) a V-cycle on these grids, and (3) an FMG-cycle on the base grid. The multigrid method exhibits spatial second-order accuracy, fast convergence, and scalability. The numerical fluxes are conserved by using a refluxing procedure in both the MHD solver and the multigrid method. Several tests are performed and the results indicate that the solutions are consistent with previously published results.

**Key words:** hydrodynamics — ISM: clouds — magnetohydrodynamics: MHD — methods: numerical — stars: formation

## 1. Introduction

Protostellar collapse is one of the most important processes in star formation; it exhibits a high dynamic range in density and spatial dimensions. Adaptive mesh refinement (AMR) is a powerful technique for performing numerical simulations requiring a high dynamic range in the mesh schemes. Local high-resolution is realized by employing grids of differing resolutions. The finer grids are inserted and their location changed according to given refinement criteria. Following the introduction of the fundamental principles of AMR by Berger & Oliger (1984) and Berger & Colella (1989), this technique is becoming widely used in astrophysical simulations.

In star formation, along with self-gravity, the magnetic field also plays an important role. Both self-gravity and magnetohydrodynamics (MHD) are therefore implemented in recent AMR codes (see the review by Klein et al. 2006).

Existing self-gravitational MHD AMR codes are generally based on Cartesian grids; although block-structured grids tend to be most often frequently, alternative approaches also exist, e.g. RAMSES (Fromang et al. 2006). In block-structured AMR, numerical cells are refined in the unit of the block, and a block is itself an ordinal uniform grid. Block-structured grids are divided into two categories: patch-oriented grids and self-similar blocks. In the former approach, a block has variable number of cells, and the shape of the block is also changed in the course of refinement. A large block containing many cells and a small block containing just a few cells can co-exist. This approach originated in the study of Berger & Colella (1989), and has been adopted in many codes: e.g., the

AMR code Orion of Berkeley (Truelove et al. 1998), Enzo (Norman & Bryan 1999), and RIEMANN (Balsara 2001). In the latter approach, all blocks contain the same number of cells, but the physical sizes of the blocks are different. This approach has also been adopted by many codes: e.g., FLASH (Fryxell et al. 2000; Banerjee & Pudritz 2006), and NIRVANA (Ziegler 2005). This approach offers advantages including relatively simple algorithms for refinement, parallelization, and vectorization. This paper also follows this latter approach. In particular, this approach enables the AMR code to implement a full multigrid (FMG)-cycle in the multigrid method for self-gravity. This scheme is an extension of the multigrid method for the nested grid approach (Matsumoto & Hanawa 2003a) to the AMR grid.

There are several ways to treat the MHD, particularly in the treatment of the  $\nabla \cdot \mathbf{B}$  term. These approaches may be categorized as (1) the constrained transport method with a staggered grid, (2) the projection scheme with a Poisson solver, and (3) the eight-wave formulation (see Tóth 2000; Balsara & Kim 2004 for a comparison of these schemes).

Recently, Dedner et al. (2002) proposed an alternative scheme for cleaning the  $\nabla \cdot \mathbf{B}$  term. This scheme has a formulation that is similar to, but distinct from, the eight-wave formulation; two additional waves transfer the  $\nabla \cdot \mathbf{B}$  error isotropically at a given speed, and the waves decay at a given rate. As a result, the error is propagated independently of the gas motion, and so is diluted. By contrast, using the eight-wave formulation, a single additional wave transfers the error at the gas velocity. The error is always propagated downstream of the gas motion, and can become stagnated at the shock wave and the center of the

collapsing cloud. The scheme of Dedner et al. (2002) is therefore adopted here.

The author has previously developed a self-gravitational MHD code with a nested grid (Matsumoto & Hanawa 2003a; Matsumoto & Hanawa 2003b; Matsumoto et al. 2004; Machida et al. 2004). In the nested grid approach, the grids are refined adaptively, while the sizes and positions of the sub-grids are fixed. The problems to which this method may be applied have therefore been restricted to those problems whose objects that require fine grid resolution are located in the center of the computational domain, e.g., Machida et al. (2006).

A self-gravitational MHD code with AMR has now, however, been developed, and this method is presented in this paper. In § 2–4, the governing equations to be solved, the rules of discretization, and the refinement algorithm are presented. In § 5, the present methods for treating the hydrodynamics and MHD of the problem are described, while in § 6, the methods of the multigrid iteration for solving self-gravity are described. In § 8, the results of several numerical tests are presented. The paper is concluded in § 9.

## 2. Governing Equations

The equations of self-gravitational, ideal hydrodynamics and MHD can be expressed in a conservative form with a source term,

$$\frac{\partial \mathbf{U}}{\partial t} + \frac{\partial \mathbf{F}_x}{\partial x} + \frac{\partial \mathbf{F}_y}{\partial y} + \frac{\partial \mathbf{F}_z}{\partial z} = \mathbf{S}, \quad (1)$$

together with Poisson's equation

$$\nabla^2 \Phi = 4\pi G \rho, \quad (2)$$

where  $\mathbf{U}$  is a vector of conservative variables,  $\mathbf{F}_x$ ,  $\mathbf{F}_y$ , and  $\mathbf{F}_z$  are numerical fluxes, and  $\mathbf{S}$  is the source term vector. In equation (2),  $\Phi$ ,  $G$ , and  $\rho$  denote the gravitational potential, the gravitational constant, and the density, respectively.

For ideal MHD with self-gravity, the vectors in equation (1) are expressed by

$$\mathbf{U} = (\rho, \rho v_x, \rho v_y, \rho v_z, B_x, B_y, B_z, \rho E)^T, \quad (3)$$

$$\mathbf{F}_x = \begin{pmatrix} \rho v_x^2 + P + |\mathbf{B}|^2/8\pi - B_x^2/4\pi \\ \rho v_x v_y - B_x B_y/4\pi \\ \rho v_x v_z - B_x B_z/4\pi \\ 0 \\ v_x B_y - v_y B_x \\ -v_z B_x + v_x B_z \\ (\rho E + P + |\mathbf{B}|^2/8\pi)v_x - B_x(\mathbf{B} \cdot \mathbf{v})/4\pi \end{pmatrix}, \quad (4)$$

$$\mathbf{S} = (0, \rho g_x, \rho g_y, \rho g_z, 0, 0, 0, \rho \mathbf{g} \cdot \mathbf{v})^T, \quad (5)$$

where  $\mathbf{v} = (v_x, v_y, v_z)^T$  represents velocity,  $\mathbf{B} = (B_x, B_y, B_z)^T$  represents the magnetic field,  $\mathbf{g} = (g_x, g_y, g_z)^T = -\nabla \Phi$  represents gravity,  $E = |\mathbf{v}|^2/2 + (\gamma - 1)^{-1}P/\rho + |\mathbf{B}|^2/8\pi\rho$  is the total energy, and  $P$  represents

pressure. The vectors  $\mathbf{F}_y$  and  $\mathbf{F}_z$  are obtained by rotating the components in  $\mathbf{F}_x$  by the right-hand rule.

For ideal hydrodynamics with self-gravity, the governing equations are obtained by setting  $\mathbf{B} = 0$  and omitting the 5th to the 7th components of equation (1) and vectors (3)–(5).

Barotropic and isothermal equations of state are also implemented in the AMR code. In these equations of state, the component corresponding to  $E$  in equation (1) and vectors (3)–(5) (the eighth component) are excluded, and  $P$  is expressed as a function of  $\rho$ .

## 3. Discretization

Equations (1) and (2) are solved by a difference scheme based on the finite-volume approach. The computational domain is divided into cells, each of size  $\Delta x \times \Delta y \times \Delta z$ . Each cell is labeled by  $(i, j, k)$ , the indices of the cell in the  $x$ ,  $y$ , and  $z$ -directions, respectively. The location of the cell center is indicated by the position vector  $\mathbf{r}_{i,j,k}$ . The conservative variables  $\mathbf{U}$ , the source term  $\mathbf{S}$ , and the gravitational potential  $\Phi$  are defined at the cell center, i.e.,  $\mathbf{U}_{i,j,k} := \mathbf{U}(\mathbf{r}_{i,j,k})$ ,  $\mathbf{S}_{i,j,k} := \mathbf{S}(\mathbf{r}_{i,j,k})$ , and  $\Phi_{i,j,k} := \Phi(\mathbf{r}_{i,j,k})$ . The numerical fluxes  $\mathbf{F}_x$ ,  $\mathbf{F}_y$ , and  $\mathbf{F}_z$  are defined at the cell surfaces with normals in the  $x$ ,  $y$ , and  $z$ -directions, respectively. For convenience, the notation of  $\mathbf{F}_{x,i\pm 1/2,j,k} := \mathbf{F}_x[\mathbf{r}_{i,j,k} \pm (\Delta x/2)\hat{\mathbf{x}}]$  is introduced, where  $\hat{\mathbf{x}}$  denotes the unit vector in the  $x$ -direction. We introduce the following notation to describe the spatial differences,

$$\partial_x Q_{i+1/2,j,k} = \frac{Q_{i+1,j,k} - Q_{i,j,k}}{\Delta x}, \quad (6)$$

$$\partial_x Q_{i,j,k} = \frac{Q_{i+1/2,j,k} - Q_{i-1/2,j,k}}{\Delta x}, \quad (7)$$

$$\partial_x^2 Q_{i,j,k} = \frac{Q_{i+1,j,k} - 2Q_{i,j,k} + Q_{i-1,j,k}}{\Delta x^2}. \quad (8)$$

The differences in the  $y$ - and  $z$ -directions are expressed in a similar manner.

## 4. Grid Refinement

A self-similar block-structured grid is adopted. Each block consists of  $N_x \times N_y \times N_z$  cells, where  $N_x$ ,  $N_y$ , and  $N_z$  denote the number of cells in the  $x$ ,  $y$ , and  $z$ -directions respectively, with all blocks having the same number of cells. The number of cells inside a block is fixed in course of calculation, but the cell width differs depending on the grid-level. The blocks are thus self-similar. A schematic diagram of a block-structured grid is shown in Figure 1. The number of cells is set at  $N_x = N_y = N_z = 8$  in this figure.

If some cells satisfy a refinement criterion, the block in which these cells lie is divided into 8 child blocks, and every cell inside the parent block is also refined into 8 child cells (see Fig. 1). The cell width of the child cells is half of the parent cell width, that is the refinement ratio is fixed at two in this implementation (in some AMRs having

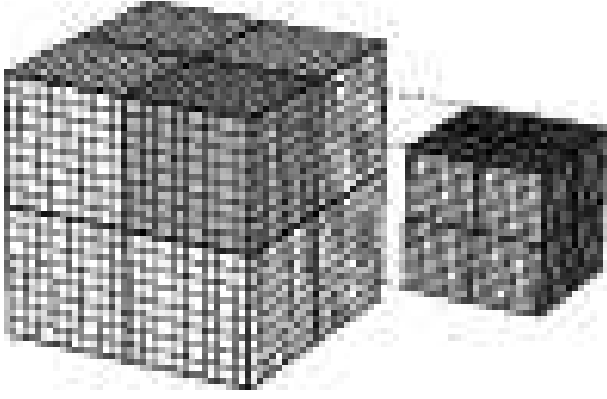


**Fig. 1.** Schematic diagram of the grid refinement process. The thick lines represent the boundaries of the blocks and the thin lines represent the boundaries of the cells. Each block consists of  $8^3$  cells in this figure. The hatched block is refined into 8 child blocks.

patch-oriented grids any refinement ratio of the power of 2 can be used). The coarsest grid-level is labeled  $\ell = 0$  (the base grid), and the finest grid-level is labeled  $\ell = \ell_{\max}$ . The  $\ell$ -th grid-level has a  $2^\ell$  times higher spatial resolution than the coarsest grid-level. The block-structured grid is managed by an octree structure; the parent (coarse) block is linked with eight fine (child) blocks. Moreover, a block is linked with its neighboring blocks. These link lists are reconstructed every time the grids are refined.

In the construction of a child block, the conservative variables of the parent cells  $\mathbf{U}_{I,J,K}^H$  are interpolated to obtain those of the child cells  $\mathbf{U}_{i,j,k}^h$ . For this purpose linear interpolation with a slope limiter is adopted,

$$\mathbf{U}_{i,j,k}^h = \mathbf{U}_{I,J,K}^H + \nabla \mathbf{U}^H \cdot (\mathbf{r}_{i,j,k}^h - \mathbf{r}_{I,J,K}^H), \quad (9)$$

where  $\mathbf{r}_{i,j,k}^h$  and  $\mathbf{r}_{I,J,K}^H$  denote the position vectors indicating the centers of the child and parent cells, respectively. The gradient inside the parent cell is slope-limited according to

$$\nabla \mathbf{U}^H = \begin{pmatrix} \min\text{mod} \left( \partial_x \mathbf{U}_{I+1/2,J,K}^H, \partial_x \mathbf{U}_{I-1/2,J,K}^H \right) \\ \min\text{mod} \left( \partial_y \mathbf{U}_{I,J+1/2,K}^H, \partial_y \mathbf{U}_{I,J-1/2,K}^H \right) \\ \min\text{mod} \left( \partial_z \mathbf{U}_{I,J,K+1/2}^H, \partial_z \mathbf{U}_{I,J,K-1/2}^H \right) \end{pmatrix}, \quad (10)$$

where  $\min\text{mod}(\cdot, \cdot)$  denotes the minmod function. Note that this interpolation conserves the conservative variables in the refinement procedure,

$$\int_{\Omega_{I,J,K}^H} \mathbf{U}^H(\mathbf{r}) d\mathbf{r} = \int_{\Omega_{i,j,k}^h} \mathbf{U}^h(\mathbf{r}) d\mathbf{r}, \quad (11)$$

where  $\Omega_{I,J,K}^H$  denotes the zone of a parent cell whose center is located at  $\mathbf{r}_{I,J,K}^H$ .

The refinement algorithm is based on that of Berger & Colella (1989), where grids of level  $\ell$  are refined using the following procedures to construct grids of level  $\ell + 1$ :

1. A block of grid-level  $\ell$  is marked if the cells inside the block satisfy a refinement criterion.

2. If blocks of grid-level  $\ell + 2$  exist, then the corresponding blocks of  $\ell$  are also marked.
3. Blocks adjacent to marked blocks are also marked, so that the grids of level  $\ell + 1$  properly nest the grids of level  $\ell + 2$ .
4. New blocks of level  $\ell + 1$  are constructed as child blocks of the marked blocks.
5. Blocks of  $\ell + 1$  are removed if their parent blocks are not marked.

These procedures are called in ascending order of grid-level, from  $\ell_{\max} - 1$  to 0.

## 5. Hydrodynamics and MHD

### 5.1. Basic Solvers

The governing MHD equations (1), which include as a special case the hydrodynamics equations, are solved on the block-structured grid described in § 4. Methods used on ordinal uniform grids can be applied to the block-structured grid if boundary conditions are properly specified for each block. A monotone upstream-centered scheme for conservation laws (MUSCL) approach and predictor-corrector method are adopted here for integration with respect to time in order to achieve a second-order accuracy in space and time (e.g., Hirsch 1990), and an unsplit approach rather than a fractional timestep approach is adopted.

The numerical flux is obtained using the linearized Riemann solver; the solvers are based on the schemes of Roe (1981) and Fukuda & Hanawa (1999). For MHD, the hyperbolic divergence cleaning of Dedner et al. (2002) is adopted for reducing  $\nabla \cdot \mathbf{B}$ . According to Dedner et al. (2002), equations (3)–(5) are then modified as follows:

$$\mathbf{U} = (\rho, \rho v_x, \rho v_y, \rho v_z, B_x, B_y, B_z, \rho E, \psi)^T, \quad (12)$$

$$\mathbf{F}_x = \begin{pmatrix} \rho v_x \\ \rho v_x^2 + P + |\mathbf{B}|^2/8\pi - B_x^2/4\pi \\ \rho v_x v_y - B_x B_y/4\pi \\ \rho v_x v_z - B_x B_z/4\pi \\ \psi \\ v_x B_y - v_y B_x \\ -v_z B_x + v_x B_z \\ (\rho E + P + |\mathbf{B}|^2/8\pi)v_x - B_x(\mathbf{B} \cdot \mathbf{v})/4\pi \\ c_h^2 B_x \end{pmatrix}, \quad (13)$$

$$\mathbf{S} = \begin{pmatrix} 0 \\ \rho g_x - (\nabla \cdot \mathbf{B})B_x/4\pi \\ \rho g_y - (\nabla \cdot \mathbf{B})B_y/4\pi \\ \rho g_z - (\nabla \cdot \mathbf{B})B_z/4\pi \\ 0 \\ 0 \\ 0 \\ \rho(\mathbf{g} \cdot \mathbf{v}) - \mathbf{B} \cdot (\nabla \psi)/4\pi \\ -(c_h/c_p)^2 \psi \end{pmatrix}, \quad (14)$$

where  $\psi$  is a scalar potential propagating a divergence error,  $c_h$  is the wave speed, and  $c_p$  is the damping rate of the wave. Note that this modification requires additional components in the basic equation, and a total of

nine waves are solved for. This approach is similar to the eight-wave formulation. In the method of Dedner et al. (2002), two additional waves transfer the  $\nabla \cdot \mathbf{B}$  error isotropically at a speed of  $c_h$ , and the waves decay at a rate of  $c_p$ . Similarly, in the eight-wave formulation, an additional wave transfers the divergence error at a gas velocity of  $\mathbf{v}$ .

In the predictor step,  $\mathbf{U}_{i,j,k}^n$  is updated to  $\mathbf{U}_{i,j,k}^{n+1/2}$  by a half time step, i.e.,

$$\begin{aligned} \mathbf{U}_{i,j,k}^{n+1/2} &= \mathbf{U}_{i,j,k}^n \\ &- \frac{\Delta t}{2} \left( \partial_x \mathbf{F}_{x,i,j,k}^n + \partial_y \mathbf{F}_{y,i,j,k}^n + \partial_z \mathbf{F}_{z,i,j,k}^n \right. \\ &\left. - \mathbf{S}_{i,j,k}^{n,*} \right), \end{aligned} \quad (15)$$

where the superscript  $n$  denotes the time level, and  $\Delta t = t^{n+1} - t^n$ . The numerical flux  $\mathbf{F}^n$ , which is defined at the cell boundaries, is calculated using the primitive variables,

$$\mathbf{Q} = (\rho, v_x, v_y, v_z, B_x, B_y, B_z, P, \psi)^T. \quad (16)$$

The numerical flux has second-order spatial accuracy due to the MUSCL extrapolation of the amplitudes of the eigenmode of the MHD waves,  $\mathbf{LU}$ , where  $\mathbf{L}$  denotes the matrix of the left eigenvector (see the appendix in Fukuda & Hanawa 1999 for details)<sup>1</sup>.

The source term  $\mathbf{S}_{i,j,k}^{n,*}$  is calculated using

$$\begin{aligned} \mathbf{S}_{i,j,k}^{n,*} &= \begin{pmatrix} 0 \\ \rho_{i,j,k}^n g_{x,i,j,k}^{n-1/2} - (\nabla \cdot \mathbf{B})_{i,j,k}^n B_{x,i,j,k}^n / 4\pi \\ \rho_{i,j,k}^n g_{y,i,j,k}^{n-1/2} - (\nabla \cdot \mathbf{B})_{i,j,k}^n B_{y,i,j,k}^n / 4\pi \\ \rho_{i,j,k}^n g_{z,i,j,k}^{n-1/2} - (\nabla \cdot \mathbf{B})_{i,j,k}^n B_{z,i,j,k}^n / 4\pi \\ 0 \\ 0 \\ 0 \\ \rho_{i,j,k}^n (\mathbf{g}_{i,j,k}^{n-1/2} \cdot \mathbf{v}_{i,j,k}^n) - \mathbf{B}_{i,j,k}^n \cdot (\nabla \psi)_{i,j,k}^n / 4\pi \\ 0 \end{pmatrix}, \end{aligned} \quad (17)$$

where  $(\nabla \cdot \mathbf{B})_{i,j,k} = \partial_x B_{x,i,j,k} + \partial_y B_{y,i,j,k} + \partial_z B_{z,i,j,k}$ , and the magnetic field defined at the cell surfaces,  $B_{x,i\pm 1/2,j,k}$ , is obtained from the ninth component of  $\mathbf{F}_{x,i\pm 1/2,j,k}$ . Similarly,  $(\nabla \psi)_{i,j,k} = (\partial_x \psi_{i,j,k}, \partial_y \psi_{i,j,k}, \partial_z \psi_{i,j,k})^T$  is obtained from the fifth to seventh components of  $\mathbf{F}_{x,i\pm 1/2,j,k}$ ,  $\mathbf{F}_{y,i,j\pm 1/2,k}$ , and  $\mathbf{F}_{z,i,j,k\pm 1/2}$ . The ninth component of the source term (14) is evaluated separately by operator splitting, in which the formal solution is used as follows,

$$\psi^{n+1/2} = \psi^{n+1/2,*} \exp \left[ -\frac{\Delta t}{2} \left( \frac{c_h}{c_p} \right)^2 \right], \quad (18)$$

where  $\psi^{n+1/2,*}$  is the ninth component of  $\mathbf{U}^{n+1/2}$  solved by equation (15). The free parameters  $c_h$  and  $c_p$  are related to the time-marching, and are described in § 5.2.

Note that gravity  $\mathbf{g}_{i,j,k}^{n-1/2}$  lags by half a time step. This slight lagging is expected to have a negligible effect on the accuracy in the predictor step, and the gravity in the previous corrector step can be reused in this predictor step (Truelove et al. 1998). This avoids an additional call of the multigrid method to solve Poisson's equation, significantly reducing the computational costs of this method.

In the corrector step, a spatially second-order numerical flux  $\mathbf{F}^{n+1/2}$  is obtained by applying MUSCL extrapolation to the amplitudes of the eigenmodes, which are converted from  $\mathbf{U}^{n+1/2}$ . Using this flux,  $\mathbf{U}_{i,j,k}^{n+1/2}$  is updated to  $\mathbf{U}_{i,j,k}^{n+1}$  by a full time step,

$$\begin{aligned} \mathbf{U}_{i,j,k}^{n+1} &= \mathbf{U}_{i,j,k}^{n+1/2} \\ &- \Delta t \left( \partial_x \mathbf{F}_{x,i,j,k}^{n+1/2} + \partial_y \mathbf{F}_{y,i,j,k}^{n+1/2} + \partial_z \mathbf{F}_{z,i,j,k}^{n+1/2} \right. \\ &\left. - \mathbf{S}_{i,j,k}^{n+1/2} \right). \end{aligned} \quad (19)$$

The source term in the corrector step is estimated at the time level  $t = t^{n+1/2}$ ,

$$\begin{aligned} \mathbf{S}_{i,j,k}^{n+1/2} &= \begin{pmatrix} 0 \\ \rho_{i,j,k}^{n+1/2} g_{x,i,j,k}^{n+1/2} - (\nabla \cdot \mathbf{B})_{i,j,k}^{n+1/2} B_{x,i,j,k}^{n+1/2} / 4\pi \\ \rho_{i,j,k}^{n+1/2} g_{y,i,j,k}^{n+1/2} - (\nabla \cdot \mathbf{B})_{i,j,k}^{n+1/2} B_{y,i,j,k}^{n+1/2} / 4\pi \\ \rho_{i,j,k}^{n+1/2} g_{z,i,j,k}^{n+1/2} - (\nabla \cdot \mathbf{B})_{i,j,k}^{n+1/2} B_{z,i,j,k}^{n+1/2} / 4\pi \\ 0 \\ 0 \\ 0 \\ \rho_{i,j,k}^{n+1/2} (\mathbf{g}_{i,j,k}^{n+1/2} \cdot \mathbf{v}_{i,j,k}^{n+1/2}) - \mathbf{B}_{i,j,k}^{n+1/2} \cdot (\nabla \psi)_{i,j,k}^{n+1/2} / 4\pi \\ 0 \end{pmatrix}, \end{aligned} \quad (20)$$

where  $\rho_{i,j,k}^{n+1/2}$  and  $\mathbf{v}_{i,j,k}^{n+1/2}$  are obtained from  $\mathbf{U}_{i,j,k}^{n+1/2}$ , and  $\mathbf{g}_{i,j,k}^{n+1/2}$  is obtained by solving Poisson's equation (2) at the half time step as follows,

$$(\nabla^2 \Phi)_{i,j,k}^{n+1/2} = 4\pi G \rho_{i,j,k}^{n+1/2}. \quad (21)$$

Poisson's equation is solved by the multigrid method, as shown in § 6, and the multigrid method prepares not only the cell-centered  $\Phi$ , but also the cell-surfaced  $\mathbf{g}$ . Gravity at the cell center  $\mathbf{g}_{i,j,k}^{n+1/2}$  is obtained by averaging the values of gravity at the cell surfaces,

$$\mathbf{g}_{i,j,k}^{n+1/2} = \frac{1}{2} \begin{pmatrix} g_{x,i+1/2,j,k}^{n+1/2} + g_{x,i-1/2,j,k}^{n+1/2} \\ g_{y,i,j+1/2,k}^{n+1/2} + g_{y,i,j-1/2,k}^{n+1/2} \\ g_{z,i,j,k+1/2}^{n+1/2} + g_{z,i,j,k-1/2}^{n+1/2} \end{pmatrix}. \quad (22)$$

Note that  $\mathbf{g}$  at a cell surface is obtained by the difference of the cell-centered  $\Phi$  (see equations [42]–[44]). Equation (22) therefore coincides with the central difference of  $\Phi$  as far as the inside of a block is concerned.

Similar to the predictor step, the ninth component of the source term is evaluated by operator splitting,

$$\psi^{n+1} = \psi^{n+1,*} \exp \left[ -\Delta t \left( \frac{c_h}{c_p} \right)^2 \right], \quad (23)$$

<sup>1</sup> For the case of the hydrodynamics, the MUSCL extrapolation is applied to the primitive variables,  $\mathbf{Q}$  in the predictor and corrector steps in this implementation.

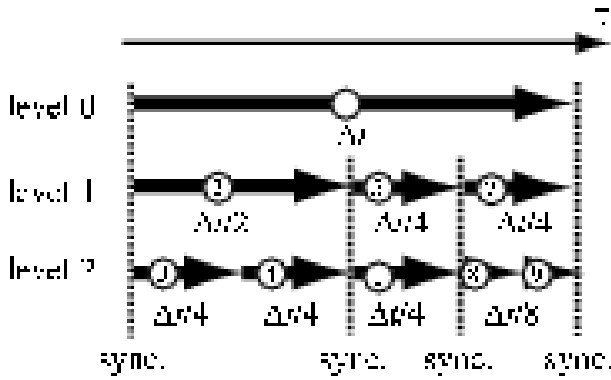


Fig. 2. Adaptive time-step scheme. The thick arrows denote time steps, while the associated numbers, ①, ②, ..., ⑤, indicate the order of time-marching.

where  $\psi^{n+1,*}$  is the ninth component of  $\mathbf{U}^{n+1}$  obtained by equation (19).

### 5.2. Time Marching

The time-marching represented by equations (15) and (19) proceeds in units at the grid-level. The code is equipped with two modes of time-marching: an adaptive and a synchronous time-step mode. Which mode is used depends on whether the gas is non-self-gravitational or self-gravitational. The adaptive time-step mode is appropriate for non-self-gravitational gases, and is based on the method of Berger & Colella (1989). In this mode, a coarser grid has a longer time step than a finer grid. In contrast, the synchronous mode is appropriate for self-gravitational gases, and every grid-level has the same time step. This is because evolution on the fine grid affects the detached coarse grid immediately due to self-gravity, and so the same time step must to be chosen for every grid-level (see discussion of Truelove et al. 1998). Note that the adaptive time-step mode could also be used for a self-gravitational gas at the expense of the first-order temporal accuracy of the scheme.

Figure 2 shows the order in which the grid-levels proceed for the adaptive time-step mode schematically. The numbers associated with the thick arrows denote the order of time-marching. Coarser grid-levels precede finer grid-levels. The fine grid-level undergoes several sub-cycles until the time level of the fine grid-level is synchronized with that of the coarse grid-level. The time step of a finer grid-level,  $\Delta t^h$ , is given by

$$\Delta t^h = \Delta t^H 2^{-n}, \quad (24)$$

$$n = \min \{ m \in \mathbb{N} \mid \Delta t^H 2^{-m} \leq \Delta t_{\text{CFL}}^h \}. \quad (25)$$

where  $\Delta t_{\text{CFL}}^h$  denotes the time step calculated directly by the CFL condition at the fine grid-level, and  $\Delta t^H$  denotes the time step at the coarser grid-level. Note that  $\Delta t^h$  is fixed at  $\Delta t^H/r$  in Berger & Colella (1989), where  $r$  denotes a refinement ratio. On the other hand, in the method presented here  $\Delta t^h$  can be equal to  $\Delta t^H/2^n$  for  $n = 0, 1, 2, \dots$ , if  $\Delta t^h$  satisfies the CFL condition. In the synchronous time-step mode, a common time step  $\Delta t$  is

used at all grid-levels, and is given by

$$\Delta t = \min_{0 \leq \ell \leq \ell_{\text{max}}} \{ \Delta t_{\text{CFL}}^\ell \}, \quad (26)$$

where  $\Delta t_{\text{CFL}}^\ell$  denotes the time step calculated by the CFL condition at grid-level  $\ell$ .

The solver described in § 5.1 includes two parameters,  $c_h$  and  $c_p$ , and these are related to the mode of the time-marching. The wave speed  $c_h$  is obtained as

$$c_h = \text{CFL} \frac{h}{\Delta t^{\ell=0}}, \quad (27)$$

where CFL denotes the CFL number, and  $\Delta t^{\ell=0}$  denotes the time step at grid-level  $\ell = 0$ . For the adaptive time-step mode,

$$h = \min_{\ell=0} \{ \Delta x^\ell, \Delta y^\ell, \Delta z^\ell \}. \quad (28)$$

while for the synchronous time-step mode,

$$h = \min_{\ell=\ell_{\text{max}}} \{ \Delta x^\ell, \Delta y^\ell, \Delta z^\ell \}, \quad (29)$$

In both cases,  $c_h$  is constant across all the grid-levels, and satisfies the CFL condition at every grid-level.

The damping rate  $c_p$  is obtained from  $c_h$ ,

$$c_p^2 = 0.18 L c_h, \quad (30)$$

where  $L$  is a scale length of a problem, and the coefficient of 0.18 is chosen according to Dedner et al. (2002). This coefficient is a free parameter specifying the ratio of the damping rate and propagation speed of  $\nabla \cdot \mathbf{B}$ . We confirmed that this selection worked well in many calculations (e.g., Machida et al. 2005a; Machida et al. 2005b) and in the numerical tests presented in this paper.

### 5.3. Boundary Condition for Ghost Cells

Each block has ghost cells overlapping with the adjacent blocks. Figure 3 shows the interface between the coarse and fine blocks in the  $x$ -direction. Two ghost cells are prepared in each direction, as indicated by the gray circles in the figure, since the MUSCL extrapolation requires two cells on both the left and right sides of a cell boundary where numerical flux is obtained.

A boundary condition is imposed on the ghost cells each time before the predictor and corrector steps proceed. When a block is adjacent to another block of the same grid-level, data is exchanged between the two blocks by a simple copy. When a block is adjacent to a coarse block, data is interpolated spatially. In addition, data is interpolated temporally if an adaptive time-step mode is used. The procedure for the boundary conditions is as follows:

1. Adjacent coarse blocks are identified.
2. Conservative variables on the coarse cells overlapping the ghost cells of a fine block are interpolated temporally to coincide with the time level of the fine grid-level. This procedure is omitted if the synchronous time-step mode is used.

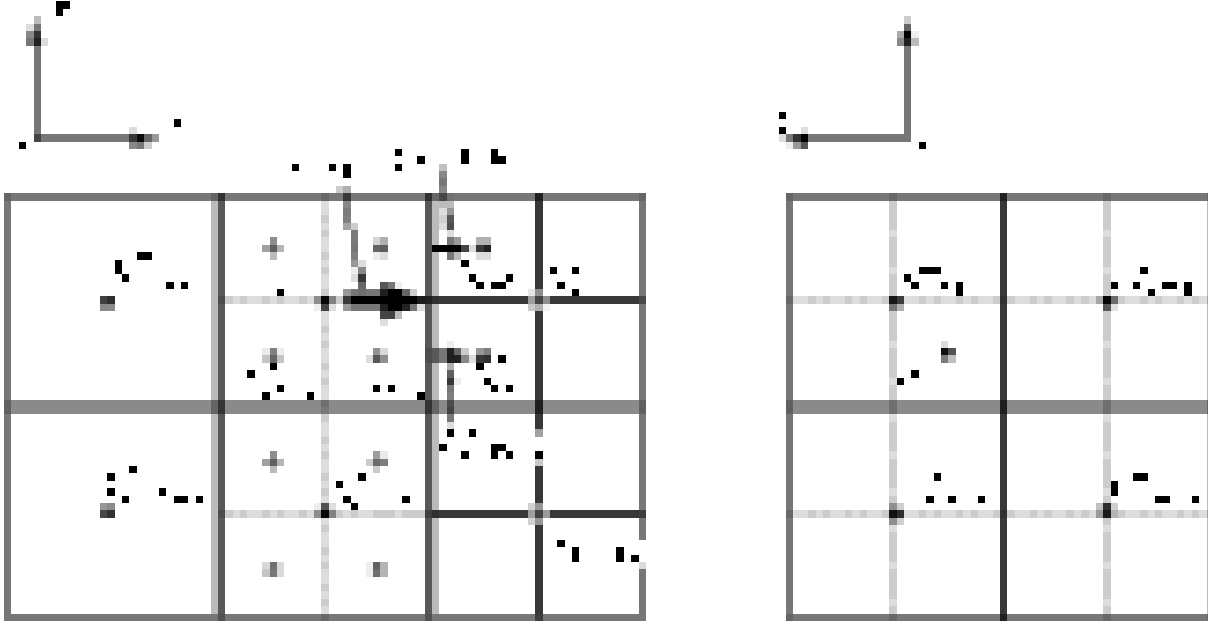


**Fig. 3.** The interface between a coarse block and a fine block. The grid points of the ghost cells for the fine block are denoted by gray circles, while the real grid points are denoted by filled circles. The arrows denote the numerical fluxes through the interface between the fine and coarse blocks.

3. The temporally interpolated variables are converted into primitive variables. They are interpolated spatially to coincide with the grid points of the ghost cells of the fine grid-level. The interpolated variables are copied into the ghost cells.
4. Adjacent blocks in the same grid-level are identified.
5. The variables of cells overlapping the ghost cells are simply copied into the ghost cells.

In the temporal interpolation, the quadratic interpolation is performed on  $\mathbf{U}^{H,n}$ ,  $\mathbf{U}^{H,n+1/2}$ , and  $\mathbf{U}^{H,n+1}$ . Note that  $\mathbf{U}^{H,n}$  and  $\mathbf{U}^{H,n+1}$  have of second-order temporal accuracy while  $\mathbf{U}^{H,n+1/2}$  is of first-order temporal accuracy. Using these variables,  $\mathbf{U}^H(t)$  in  $t^n \leq t \leq t^{n+1}$  is interpolated as,

$$\mathbf{U}^H(t) = \left( \mathbf{U}^{H,n+1} - \mathbf{U}^{(1),H,n+1} \right) \left( \frac{t - t^n}{t^{n+1} - t^n} \right)^2 + \frac{(t^{n+1} - t)\mathbf{U}^{H,n} + (t - t^n)\mathbf{U}^{(1),H,n+1}}{t^{n+1} - t^n}, \quad (31)$$

where  $\mathbf{U}^{(1),H,n+1}$  denotes the conservative variables of first-order accuracy at the time level  $t^{n+1}$ , defined as,

$$\mathbf{U}^{(1),H,n+1} = 2\mathbf{U}^{H,n+1/2} - \mathbf{U}^{H,n}. \quad (32)$$

A slope-limited gradient is adopted for the spatial interpolation. In Figure 3, the gradient of the primitive variables inside the cell  $(I, J, K)$  is evaluated using

$$\nabla \mathbf{Q}^H = \begin{pmatrix} \partial_x \mathbf{Q}_{I-1/2, J, K}^H \\ \min\text{mod} \left( \partial_y \mathbf{Q}_{I, J+1/2, K}^H, \partial_y \mathbf{Q}_{I, J-1/2, K}^H \right) \\ \min\text{mod} \left( \partial_z \mathbf{Q}_{I, J, K+1/2}^H, \partial_z \mathbf{Q}_{I, J, K-1/2}^H \right) \end{pmatrix}. \quad (33)$$

It may be noted that equation (33) describes a simple interpolation in the normal direction, with a slope-limited interpolation in the transverse directions.

#### 5.4. Refluxing at the Interfaces

Refluxing was introduced by Berger & Colella (1989), and has often been used in standard implementations of AMRs. This technique maintains consistency between the fine and coarse grid-levels during time-marching, and ensures that conservation laws, e.g., mass conservation, are satisfied.

As shown in Figure 3,  $\mathbf{U}_{I,J,K}^H$  is updated using  $\mathbf{F}_{x,I+1/2,J,K}^H$ , while  $\mathbf{U}_{i,\hat{j},\hat{k}}^h$  is updated using  $\mathbf{F}_{x,i-1/2,\hat{j},\hat{k}}^{h,n}$  through several sub-cycles until the fine grid-level catches up with the coarse grid-level, where  $\hat{j} \in [j, j+1]$ ,  $\hat{k} \in [k, k+1]$ , and  $n$  denotes the index of the sub-cycles of the fine grid-level. Obviously,  $\mathbf{F}_{x,I+1/2,J,K}^H \Delta S^H \Delta t^H$  should equal  $\sum_{\hat{j},\hat{k},n} \mathbf{F}_{x,i-1/2,\hat{j},\hat{k}}^{h,n} \Delta S^h \Delta t^{h,n}$  to ensure that the conservation laws are satisfied, where  $\Delta S^H = \Delta y^H \Delta z^H$  and  $\Delta S^h = \Delta y^h \Delta z^h$ . In refluxing,  $\mathbf{U}_{I,J,K}^H$  is re-calculated, taking account of the difference between  $\mathbf{F}_{x,I+1/2,J,K}^H \Delta S^H \Delta t^H$  and  $\sum_{\hat{j},\hat{k},n} \mathbf{F}_{x,i-1/2,\hat{j},\hat{k}}^{h,n} \Delta S^h \Delta t^{h,n}$ . More explicitly, as indicated in Figure 4, the refluxing procedure updates  $\mathbf{U}^{H,*}$  to  $\mathbf{U}^H$  according to

$$\mathbf{U}^H = \mathbf{U}^{H,*} - \frac{1}{\Delta V^H} \left( \sum_n \sum_{\text{surface}} \mathbf{F}_x^{h,n} \Delta t^{h,n} \Delta S^h - \mathbf{F}_x^H \Delta t^H \Delta S^H \right), \quad (34)$$

where

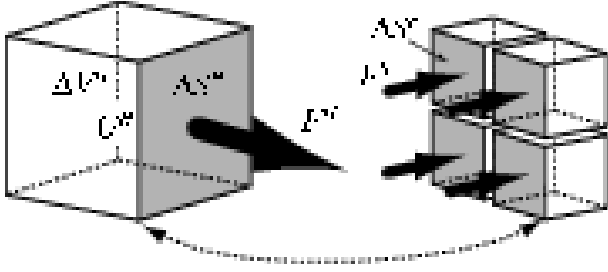


**Fig. 4.** Refluxing procedure at the interface between fine and coarse cells.

$$\sum_n \Delta t^{h,n} = \Delta t^H, \quad (35)$$

$$\sum_{\text{surface}} \Delta S^h = \Delta S^H, \quad (36)$$

and  $\Delta V^H$  denotes the volume of the coarse cell.

## 6. Multigrid Method for Self-gravity

### 6.1. Multigrid Cycles

The multigrid method is widely used in many AMRs for solving Poisson's equation. In many AMRs, a solution converges by means of the V-cycle on the grids of AMR hierarchy, and the FMG-cycle on a uniform base grid. By contrast, the multigrid method presented here uses not only V-cycles, but also FMG-cycles on the grids of the AMR hierarchy. An FMG-cycle on the hierarchical grids is also implemented in the approach of Matsumoto & Hanawa (2003a), and the same strategy is adopted here.

Figure 5 shows the grids used in the multigrid cycles for the case  $N_x = N_y = N_z = 8$ . For convenience, a grid is labeled by

$$\Omega_\ell^m \quad \text{with } \ell \in [0, \ell_{\max}] \text{ and } m \in [0, m_{\max}], \quad (37)$$

where  $\ell$  and  $m$  denote the grid-level of the AMR hierarchy and the coarsening level, respectively. For example, the hatched grid in Figure 5e is labeled as  $\Omega_1^2$ , where the grid of  $\ell = 1$  is coarsened by a factor  $2^2$ . The coarsening level of all the grids shown in Figure 5a is  $m = 0$ , while that of the grids shown in Figure 5b is  $m = 1$ , irrespective of the grid-level  $\ell$ . In addition a composite grid is defined as

$$\hat{\Omega}^m := \Omega_0^m \cup \dots \cup \Omega_{\ell_{\max}}^m. \quad (38)$$

For example, the composite grids shown in Figures 5a, 5b, and 5c are expressed as  $\hat{\Omega}^0$ ,  $\hat{\Omega}^1$ , and  $\hat{\Omega}^2$ , respectively.

An overview of the cycles used by the present numerical method is now presented. First, the solution on  $\hat{\Omega}^m$  for  $0 \leq m \leq \hat{m}_{\max}$  converges under FMG-cycles, as shown in Figures 5a-5c and 6a. The maximum coarsening level in the FMG-cycle is given by  $\hat{m}_{\max} = \log_2 \min(N_x, N_y, N_z) - 1$ . In other words, the grid is coarsened until the number of the cells per block is decreased up to two in at least one direction. At the bottom of the FMG-cycle, which is marked by V in Figure 6a, the solution then converges on  $\Omega_\ell^m$  for  $0 \leq \ell \leq \ell_{\max}$  and  $m = \hat{m}_{\max}$  under V-cycles (the hatched grids in Figures 5d-5f). Typically, only one iteration of

the V-cycle is sufficient, although, for reference, two cycles of the V-cycle are illustrated in Figure 6b. At the bottom of the V-cycle, which is marked by B in Figure 6b, the solution on the coarsened base grid  $\Omega_0^m$  for  $m \geq \hat{m}_{\max}$  converges under FMG-cycles, as shown in Figures 5g-5i and 6c. Finally, at the bottom of the FMG-cycle on the base grid, which is marked by E in Figure 6c, an exact solution is given according to the boundary conditions, since there is only one cell in the computational domain.

Note that the computation at  $\hat{\Omega}^0$  of the FMG-cycle accounts for most of the computational time of the multigrid method, because the number of cells in  $\hat{\Omega}^0$  dominates all others. The number of cells decreases by a factor of  $1/8$  every time the grids are coarsened. This indicates that the computation on  $\hat{\Omega}^0$  dominates the overall computational cost, and this scheme is scalable to the number of cells in a similar way as the hydrodynamics scheme (see also Matsumoto & Hanawa 2003a).

### 6.2. Smoothing

The red-black Gauss-Seidel iteration is adopted as a smoothing procedure. Conventional red-black Gauss-Seidel iteration can be applied only to a uniform grid. This iteration scheme is therefore modified so that it can be applied to composite grids, in which grids with different resolutions co-exist.

The discretization of Poisson's equation on the composite grids is now described. Poisson's equation can be expressed as a set of two equations,

$$\nabla \cdot \mathbf{g} = -4\pi G\rho, \quad (39)$$

$$\mathbf{g} = -\nabla\Phi. \quad (40)$$

These equations are discretized as

$$\partial_x g_{x,i,j,k} + \partial_y g_{y,i,j,k} + \partial_z g_{z,i,j,k} = -4\pi G\rho_{i,j,k}, \quad (41)$$

$$g_{x,i+1/2,j,k} = -\partial_x \Phi_{i+1/2,j,k}, \quad (42)$$

$$g_{y,i,j+1/2,k} = -\partial_y \Phi_{i,j+1/2,k}, \quad (43)$$

$$g_{z,i,j,k+1/2} = -\partial_z \Phi_{i,j,k+1/2}, \quad (44)$$

where  $g_{x,i+1/2,j,k}$ ,  $g_{y,i,j+1/2,k}$ , and  $g_{z,i,j,k+1/2}$  are the components of gravity defined on the cell surfaces.

Considering the fine cells adjacent to the interface between the fine and coarse cells in Figure 7, the potential on the ghost cell,  $\Phi^B$  is required in order to obtain  $g_{x,i-1/2,j,k}^h$ . The potential on the ghost cell is given by,

$$\Phi^B = \frac{10\Phi_{i,j,k}^h + 8\Phi^* - 3\Phi_{i+1,j,k}^h}{15}, \quad (45)$$

$$\Phi^* = \frac{9\Phi_{I,J,K}^H + 3(\Phi_{I,J,K-1}^H + \Phi_{I,J-1,K}^H) + \Phi_{I,J-1,K-1}^H}{16}, \quad (46)$$

where  $\Phi^B$  is obtained by quadratic interpolation in the  $x$ -direction, and  $\Phi^*$  is obtained by bilinear interpolation in the  $y-z$  plane. The quadratic interpolation in the direction normal to the interface satisfies the necessary conditions for so-called conservative interpolation (see Trottenberg, Oosterlee, & Schüller 2001). Using this

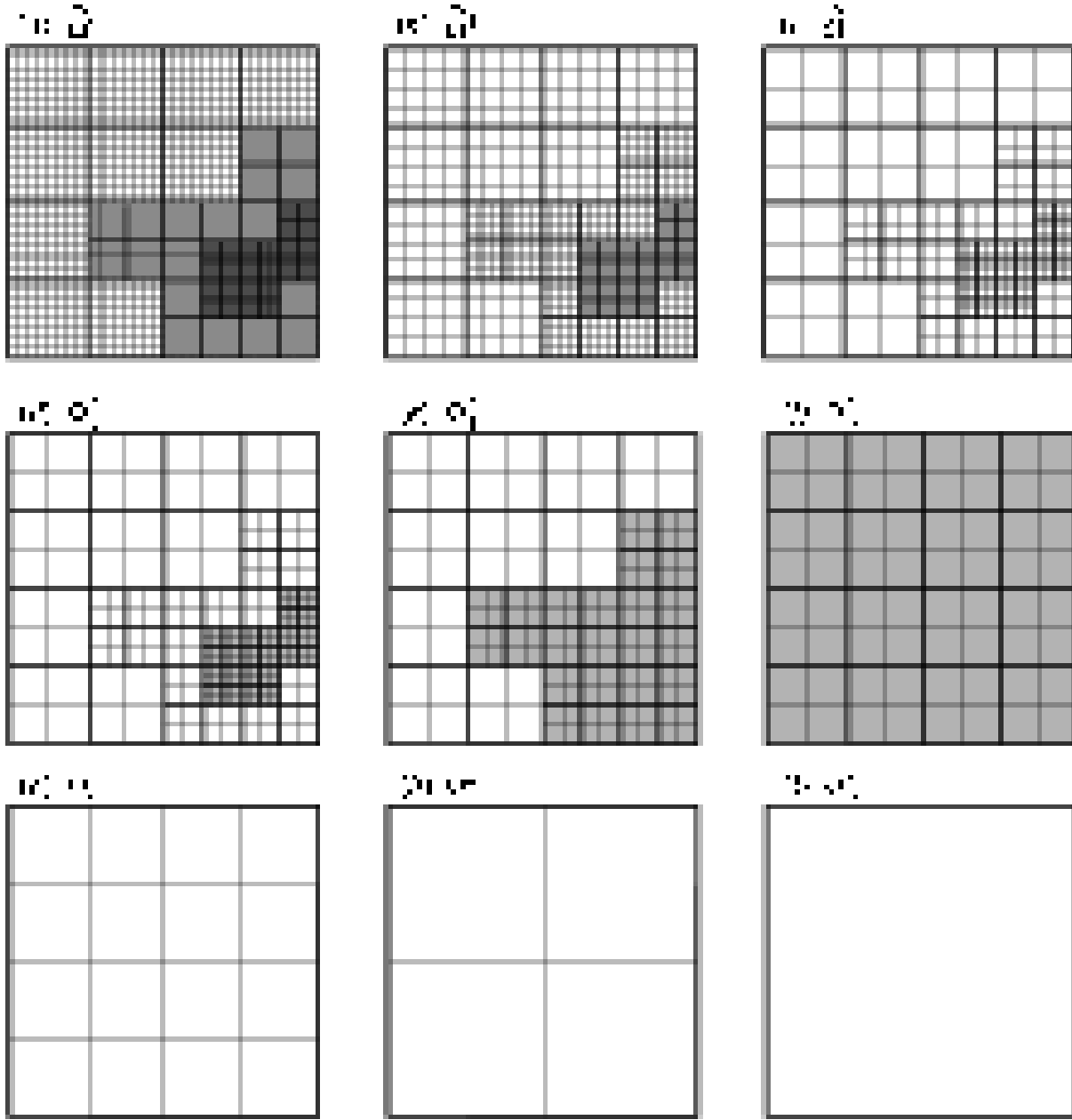


**Fig. 5.** Schematic diagram of the coarsening of grids in the multigrid method. The cell-boundaries and block-boundaries are denoted by thin and thick lines, respectively. (a–c) Coarsening of grids in the FMG-cycle on the AMR hierarchy. The number of the cells per block decreases up to  $2^3$ . (d–f) V-cycle on the AMR hierarchy. The solution converges sequentially on the hatched blocks. (g–i) Coarsening of grids in the FMG-cycle on the uniform base grid.

procedure, the components of gravity of the fine cells adjacent to coarse cells are obtained.

For the coarse cells adjacent to fine cells, the gravity at the interface is given by summing the gravity on the corresponding cell surfaces of the fine cells. For the example of Figure 7, such a coarse gravity is given by,

$$g_{x,I+1/2,J,K}^H = \frac{1}{4} \sum_{\hat{j}=j}^{j+1} \sum_{\hat{k}=k}^{k+1} g_{x,i-1/2,\hat{j},\hat{k}}^h \quad (47)$$

instead of  $g_{x,I+1/2,J,K}^H = \partial_x \Phi_{I+1/2,J,K}^H$ . This is a similar

strategy to the refluxing described in § 5.4, and ensures that the solution satisfies Gauss's theorem; when the normal component of gravity is summed over the surfaces of any cell, the sum equals the mass contained by the cell multiplied by  $4\pi G$ ,

$$\sum_{\text{surface}} \mathbf{g} \cdot \Delta \mathbf{S} = -4\pi G \rho \Delta V, \quad (48)$$

where  $\Delta V$  denotes the volume of the cell, and  $\Delta \mathbf{S}$  denotes the vector of the cross-section of the cell in the direction normal to the cell surface. We also confirmed that refluxing the gravity is necessary for second-order accuracy by



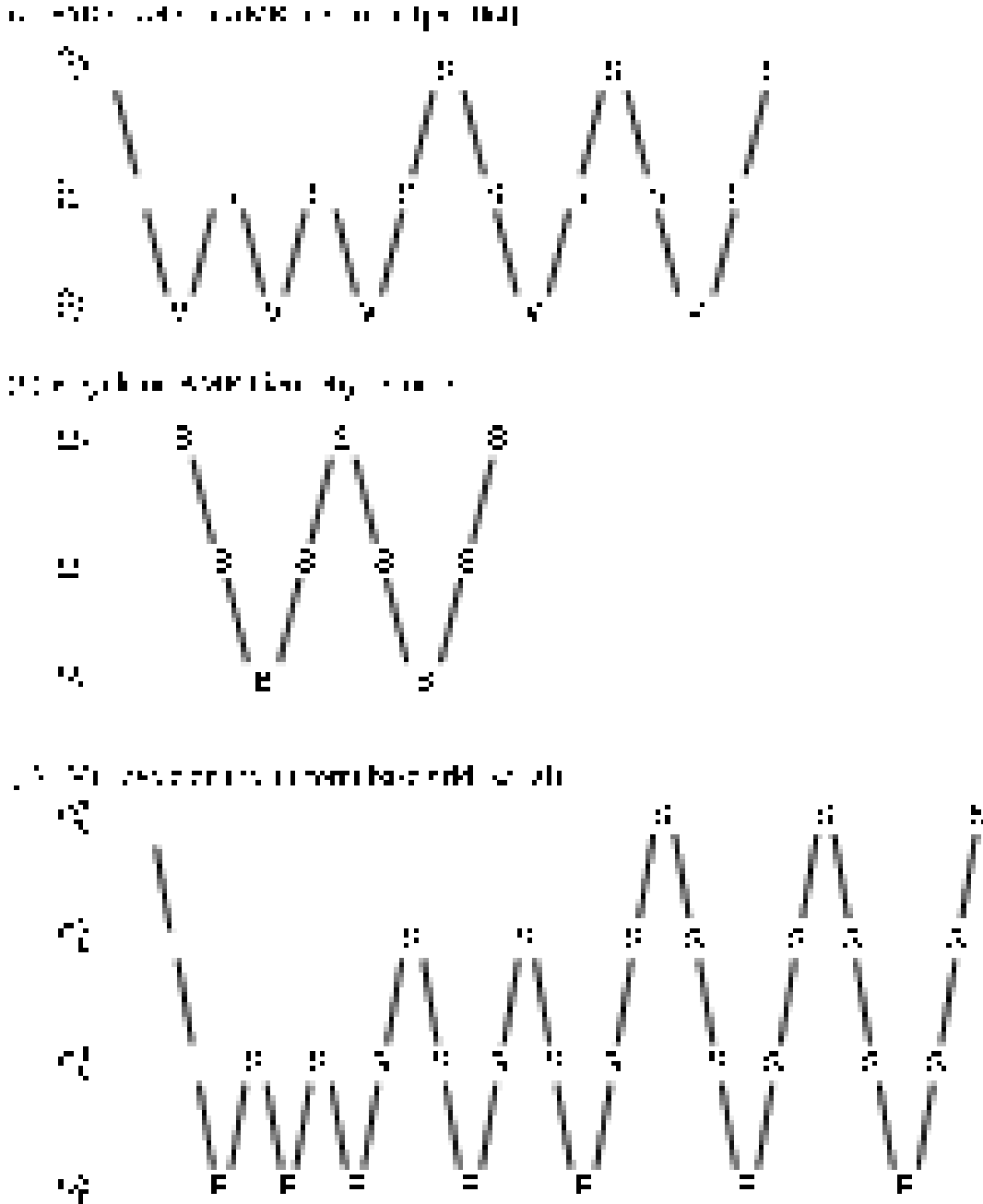


**Fig. 6.** Schematic diagram of the multigrid cycles. The lines pointing diagonally downwards from left to right denote the restriction operators, while the lines pointing diagonally upwards from left to right denote the prolongation operators. The S symbols denote the smoothing operators. The V symbols in panel *a* denote the V-cycles on the AMR hierarchy shown in panel *b*. The B symbols in panel *b* denote the FMG-cycles on the uniform base grid shown in panel *c*. At the point denoted by E, an exact solution is obtained according to the boundary conditions.

a convergence test (see § 8.5).

This refluxing of the gravity is adopted only for the FMG-cycle on the composite grids shown in Figure 6*a*, in which the solution converges simultaneously on  $\Omega_\ell^m$  over the grid-levels  $\ell$ . The refluxing of gravity is not adopted in the V-cycle, since the solution converges sequentially over the grid-levels,

According to the discretization of equation (41), the Gauss-Seidel iteration is expressed as,

$$\Phi_{i,j,k}^{\text{new}} = \Phi_{i,j,k} - \frac{h^2}{6} R_{i,j,k}, \quad (49)$$

$$\begin{aligned} R_{i,j,k} &:= \partial_x g_{x,i,j,k} + \partial_y g_{y,i,j,k} + \partial_z g_{z,i,j,k} + 4\pi G \rho_{z,i,j,k} \\ &= -\mathcal{L}\Phi_{i,j,k} + 4\pi G \rho_{z,i,j,k}, \end{aligned} \quad (50)$$

where  $h$  denotes the cell width,  $R_{i,j,k}$  denotes the residual, and  $\mathcal{L}$  denotes the Laplacian operator. Equation (49) updates  $\Phi_{i,j,k}$  to  $\Phi_{i,j,k}^{\text{new}}$  at every iteration. Typically only two iterations are required for the FMG-cycle, and one itera-

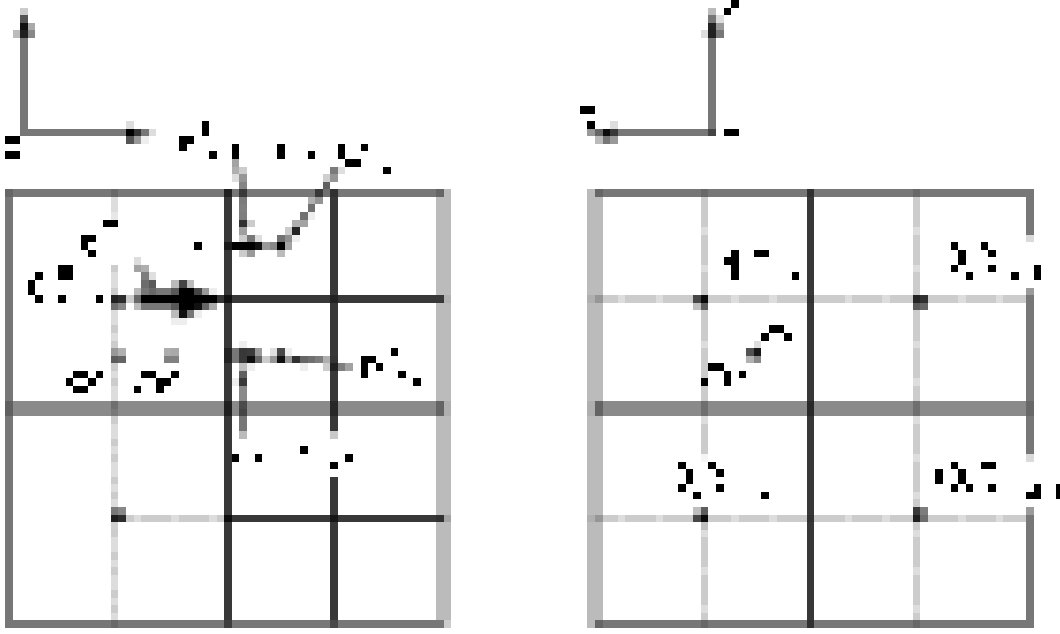


Fig. 7. Interface between the fine and coarse cells for the multigrid method.

tion for the V-cycle. Hereafter,  $\Phi_{i,j,k}^{\text{new}} = \mathcal{L}_{\text{GS}}^{-1}(\Phi_{i,j,k}, \rho_{i,j,k})$  refers to the Gauss-Seidel iteration given by equations (49) and (50).

### 6.3. Prolongation and Restriction

The full-weight prolongation is adopted here, and is given by

$$\begin{aligned} \Phi_{i,j,k}^h &= \mathcal{I}_H^h \Phi^H \\ &= \frac{1}{64} \left[ 27\Phi_{I,J,K}^H + \Phi_{I\pm 1, J\pm 1, K\pm 1}^H \right. \\ &\quad + 9(\Phi_{I\pm 1, J, K}^H + \Phi_{I, J\pm 1, K}^H + \Phi_{I, J, K\pm 1}^H) \\ &\quad \left. + 3(\Phi_{I, J\pm 1, K\pm 1}^H + \Phi_{I\pm 1, J, K\pm 1}^H + \Phi_{I\pm 1, J\pm 1, K}^H) \right], \end{aligned} \quad (51)$$

where  $(I, J, K)$  indicates a coarse cell overlapping with a fine cell  $(i, j, k)$ , and the sign of  $\pm$  depends on the parity of  $i, j$ , and  $k$ .

The restriction procedure is performed by averaging the values of the fine cells  $(i, j, k)$  which overlap the corresponding coarse cell  $(I, J, K)$ ,

$$\Phi_{I,J,K}^H = \mathcal{I}_h^H \Phi^h = \frac{1}{8} \sum_{\hat{i}=i}^{i+1} \sum_{\hat{j}=j}^{j+1} \sum_{\hat{k}=k}^{k+1} \Phi_{\hat{i},\hat{j},\hat{k}}^h, \quad (52)$$

The prolongation and restriction introduced above is used in common with all the multigrid cycles.

### 6.4. FMG-Cycle on AMR hierarchy

An FMG-cycle based on the standard algorithm of the FMG-cycle for linear equations (see e.g., Press & Teukolsky 1991) is implemented on the composite grids of the AMR hierarchy, because the basic operators are prepared on the composite grids. The smoothing, prolongation, and restriction procedures are given by equa-

tions (49), (52), and (52), respectively. In the smoothing procedure, the refluxing of the gravity is performed according to equation (47). In the prolongation, the variables on  $\Omega_\ell^m$  are transferred onto  $\Omega_\ell^{m-1}$ . Similarly, the restriction procedure transfers variables on  $\Omega_\ell^m$  onto  $\Omega_\ell^{m+1}$ . The overlap of coarse grids on fine grids,  $\Omega_\ell^m \cap \Omega_{\ell+1}^m$ , is therefore not taken into account in the FMG-cycle.

### 6.5. V-Cycle on AMR hierarchy

In the V-cycle, the multilevel adaptive technique (MLAT) is adopted by using the full approximation scheme (FAS) (see e.g., Trottenberg, Oosterlee, & Schüller 2001). The solution is iterated towards convergence on  $\Omega_\ell^m$ , where the boundary condition at  $\partial\Omega_\ell^m$  is obtained from  $\Omega_{\ell-1}^m$  according to equations (45) and (46). The prolongation procedure transfers variables from  $\Omega_{\ell-1}^m$  to  $\Omega_\ell^m$ , while the restriction procedure transfers variables from  $\Omega_\ell^m$  to  $\Omega_{\ell-1}^m$ .

We now describe the method of the V-cycle in terms of the fine and coarse grids,  $\Omega_\ell^m$  and  $\Omega_{\ell-1}^m$ . As a pre-smoothing procedure, the smoothing procedure is applied to the initial guess of  $\Phi^h$  on  $\Omega_\ell^m$ ,

$$\bar{\Phi}^h = \mathcal{L}_{\text{GS}}^{-1}(\Phi^h, \rho^h). \quad (53)$$

The density on  $\Omega_{\ell-1}^m$  is then obtained as

$$\rho^{H,*} := \begin{cases} \mathcal{I}_h^H \rho^h + \tau & \text{on } \Omega_{\ell-1}^m \cap \Omega_\ell^m \\ \rho^H & \text{on the remaining part of } \Omega_{\ell-1}^m \end{cases}, \quad (54)$$

where

$$\tau = \mathcal{L}^H \mathcal{I}_h^H \bar{\Phi}^h - \mathcal{I}_h^H \mathcal{L}^h \bar{\Phi}^h, \quad (55)$$

is the so-called  $\tau$ -correction. The initial guess on  $\Omega_{\ell-1}^m$  is given by,

$$\Phi^{H,*} := \begin{cases} \mathcal{I}_h^H \bar{\Phi}^h & \text{on } \Omega_{\ell-1}^m \cap \Omega_\ell^m \\ \Phi^H & \text{on the remaining part of } \Omega_{\ell-1}^m \end{cases}. \quad (56)$$

Using  $\rho^{H,*}$  and  $\Phi^{H,*}$ , the approximate solution  $\hat{\Phi}^H$  is obtained from the coarser grids. Then,  $\bar{\Phi}^h$  is updated to  $\hat{\Phi}^h$  on  $\Omega_\ell^m$  according to,

$$\hat{\Phi}^h = \bar{\Phi}^h + \mathcal{I}_h^h \left( \hat{\Phi}^H - \mathcal{I}_h^H \bar{\Phi}^h \right), \quad (57)$$

Finally, post-smoothing is applied to  $\hat{\Phi}^h$ ,

$$\Phi^{h,\text{new}} = \mathcal{L}_{\text{GS}}^{-1} \left( \hat{\Phi}^h, \rho^h \right). \quad (58)$$

Thus, by this algorithm, the initial guess  $\Phi^h$  is updated to  $\Phi^{h,\text{new}}$ .

### 6.6. Utilization of Multigrid Method

The front-end of the multigrid method described here is the FMG-cycle on the AMR hierarchy. Given density  $\rho$ , the boundary condition for  $\Phi$ , and the initial guess  $\Phi^0$ , the FMG-cycle is called iteratively, and  $\Phi^n$  is updated to  $\Phi^{n+1}$  by means of the following procedure,

$$R_{i,j,k} = 4\pi G \rho_{i,j,k} - \mathcal{L} \Phi_{i,j,k}^n, \quad (59)$$

$$\Phi_{i,j,k}^{n+1} = \Phi_{i,j,k}^n + \mathcal{L}_{\text{FMG}}^{-1} (0, R_{i,j,k}), \quad (60)$$

where  $\mathcal{L}_{\text{FMG}}^{-1}(\Phi, \rho)$  denotes the Poisson solver of the FMG-cycle on the AMR hierarchy with initial guess  $\Phi$  and the right-hand side of Poisson's equation  $\rho$ . The refluxing of the gravity is implemented in both the  $\mathcal{L}$  and  $\mathcal{L}_{\text{FMG}}^{-1}$  operators. The FMG-cycle  $\mathcal{L}_{\text{FMG}}^{-1}$  is always called for the fixed boundary condition of zero, because the boundary condition is transmitted to the residual  $R$  according to equation (59).

The solution converges under the iterative cycle of equations (59) and (60), reducing the absolute value of the residual  $|R|$ . In the problem of cloud collapse, the solution of  $\Phi$  in the previous time step is adopted as the initial guess, and just a single cycle reduces the residual typically by  $|Rh^2|_{\text{max}} / (4\pi G \rho h^2)_{\text{max}} \sim 10^{-4}$ .

## 7. Parallelization and Vectorization

The code is written entirely in Fortran90, and parallelized by the MPI library. The data is partitioned into the computational nodes used for the parallel calculation in units of the blocks; all cells within a given block are assigned to the same node. For a given grid-level, all the blocks are ordered by means of the Peano-Hilbert space filling curve, and the blocks are then assigned to the nodes according to this order. The vectorization in block units is computationally intensive. Since a block has  $N_x \times N_y \times N_z$  cells, the vector-length is of the order  $N_x \times N_y \times N_z$ . The block sizes,  $N_x$ ,  $N_y$ , and  $N_z$  are set at the initial configuration, and the choice of the block size depends on the machine. In the typical case  $N_x = N_y = N_z = 8$  is chosen, and the vector-length is therefore about 512, which is acceptable for the vector processor used in the calculations. In the next section, convergence tests are performed by changing the block sizes,  $N_x$ ,  $N_y$ , and  $N_z$ .

## 8. Numerical Tests

### 8.1. Simple Linearized MHD Waves

Convergence tests for the linearized MHD waves (fast, slow, Alfvén, and entropy waves) are shown. Following Crockett et al. (2005) and Gardiner & Stone (2005), the waves propagation at a slope of 2:1 is performed on uniform grids and AMR hierarchical grids in the  $x-y$  plane.

The unperturbed state is set at,  $\rho_0 = 1$ ,  $P_0 = 1$ ,  $\mathbf{v}_0 = 0$ , and  $\mathbf{B}_0 = \sqrt{4\pi} \left( \frac{1}{\sqrt{2}}, \frac{1}{\sqrt{2}}, 0 \right)^T$  in  $x, y \in [0, 1]$ . The specific heat ratio is  $\gamma = 5/3$ . All the linearized MHD waves have wave number of  $\mathbf{k} = 2\pi(2, 1, 0)^T$ . The wavelength is therefore  $\lambda = 1/\sqrt{5}$ , and the computational domain includes two net waves (Fig. 8).

The initial perturbations of the fast and slow waves are set based on the eigenmode, such as,

$$\begin{pmatrix} \delta\rho \\ \delta v_{\parallel} \\ \delta v_{\perp} \\ \delta B_{\perp} \\ \delta P \end{pmatrix} = \begin{pmatrix} \rho_0 \\ c_{F/S} \\ -\frac{B_{\parallel} B_{\perp}}{4\pi\rho_0} \frac{c_{F/S}}{c_{F/S}^2 - c_a^2} \\ B_{\perp} \frac{c_{F/S}^2}{c_{F/S}^2 - c_a^2} \\ (\gamma - 1) \left( \rho_0 c_{F/S}^2 - \frac{B_{\perp} \delta B_{\perp}}{4\pi} \right) - (\gamma - 2) \rho c_s^2 \end{pmatrix} \times \delta_{\text{pert}} \sin(\mathbf{k} \cdot \mathbf{r}), \quad (61)$$

$$c_{F/S}^2 = \frac{1}{2} \left[ c_s^2 + c_A^2 \pm \sqrt{(c_s^2 + c_A^2)^2 - 4c_s^2 c_A^2} \right] \quad (62)$$

$$c_a^2 = \frac{B_{\parallel}^2}{4\pi\rho_0} \quad (63)$$

$$c_A^2 = \frac{B_0^2}{4\pi\rho_0} \quad (64)$$

$$c_s^2 = \gamma \frac{P_0}{\rho_0} \quad (65)$$

where  $v_{\parallel}$  and  $v_{\perp}$  denote the parallel and perpendicular components of  $\mathbf{v}$  with respect to  $\mathbf{k}$ . Similarly,  $B_{\parallel}$  and  $B_{\perp}$  denote the parallel and perpendicular components of  $\mathbf{B}$  with respect to  $\mathbf{k}$ . The subscripts  $F$  and  $S$  represent the fast and slow waves. The amplitude of the perturbation is set at  $\delta_{\text{pert}} = 10^{-5}$ . For the Alfvén wave, the initial perturbation is set as,

$$\begin{pmatrix} \delta v_z \\ \delta B_z \end{pmatrix} = \begin{pmatrix} c_A \\ -B_0 \end{pmatrix} \delta_{\text{pert}} \sin(\mathbf{k} \cdot \mathbf{r}). \quad (66)$$

The entropy wave is a simple advection wave, and the perturbation is imposed only on the density,

$$\delta\rho = \rho_0 \delta_{\text{pert}} \sin(\mathbf{k} \cdot \mathbf{r}), \quad (67)$$

and the velocity of the unperturbed state is set to,

$$\mathbf{v}_0 = \frac{\mathbf{k}}{k}, \quad (68)$$

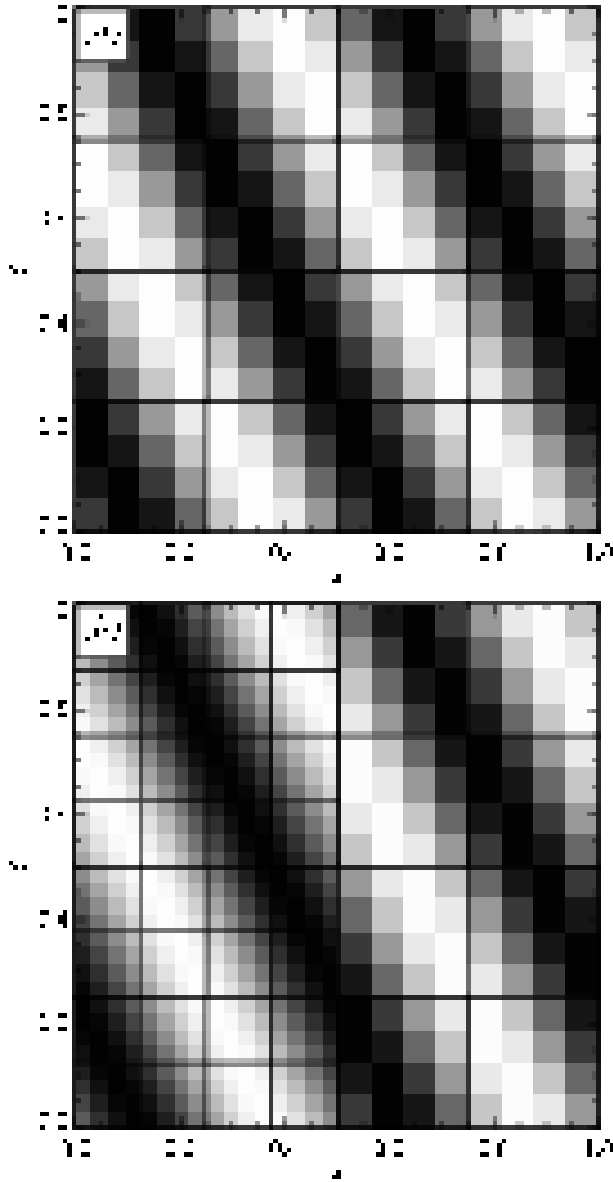


**Fig. 8.** Initial conditions for propagation of the simple linearized MHD waves on (a) the uniform grid and (b) the AMR hierarchical grid. The rectangles denote the block distributions and each block contains  $N_x \times N_y = 4^2$  cells.

rather than  $v_0 = 0$ .

Figure 8 shows the wave patterns at the initial conditions and the block distribution. The wave propagates in the upper right direction. The uniform grid consists of  $4 \times 4$  blocks of the base grid  $\ell = 0$  (Fig. 8a). In the AMR hierarchical grid (Fig. 8b), the region of  $x \leq 0.5$  is covered by fine grids of  $\ell = 1$ . In this test, the AMR hierarchical grid is static; the block distribution shown in Figure 8 is preserved in the course of the calculations in order to investigate wave propagation on the coexistence of the fine and coarse cells. For both the uniform and AMR grids, the periodic boundary condition is imposed on the  $x = 0, 1$  and  $y = 0, 1$ . The three-dimensional code is applied to this problem even though it has a two-dimensional symmetry,

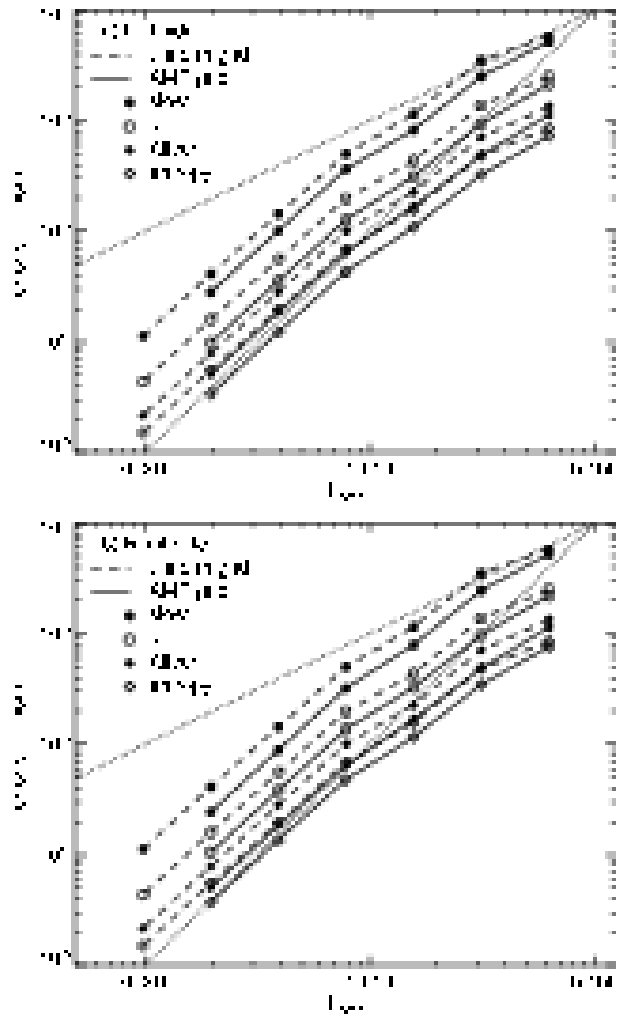


**Fig. 9.**  $L_1$  norm of error as a function of cell width of the coarsest grid  $\ell = 0$ ,  $h_{\text{base}}$ , for (a) the left side ( $x \leq 0.5$ ) and (b) the right side ( $x \geq 0.5$ ) of the computational domain. The lines with filled circles, open circles, filled diamonds, and open diamonds denote errors for slow, fast, Alfvén and entropy waves, respectively. The solid and dashed lines are for the AMR and uniform grids, respectively. The dotted lines indicate the relationship of errors in proportion to  $h_{\text{base}}^2$ , and that in proportion to  $h_{\text{base}}$ .

with all the variables being constant in the  $z$ -direction.

We performed the convergence test by changing the cell number inside a block as  $4 \leq N_x, N_y \leq 256$  for the uniform grids, and  $4 \leq N_x, N_y \leq 128$  for the AMR grids. This corresponds to a change in the resolution from  $h = 1/16$  to  $1/1024$  for the uniform grids, from  $h = 1/16$  to  $1/512$  for grid-level  $\ell = 0$  of the AMR grids, and from  $h = 1/32$  to  $1/1024$  for grid-level  $\ell = 1$ , respectively, where  $h = \Delta x = \Delta y$ . Each run is halted when a wave is propagated by a distance of three wavelengths so that all the waves sweep the entire computational domain. A  $L_1$  norm of the error is estimated by

$$L_1 = \sum_{i,j,m} \left| U_{i,j}^m - U_{i,j}^{m,0} \right| \Delta S_{i,j} \quad (69)$$

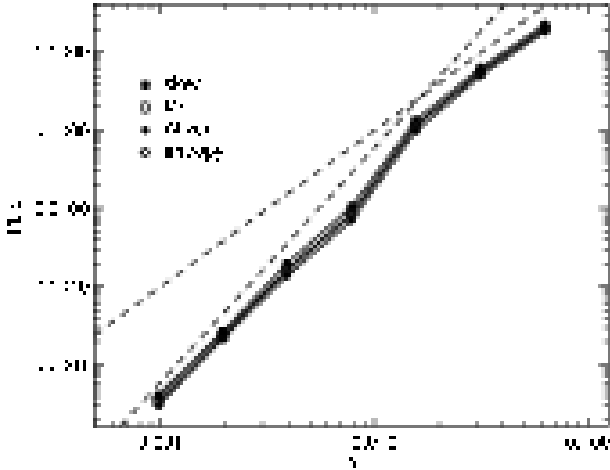


**Fig. 10.** Decay rate as a function of cell width for slow, fast, Alfvén, and entropy waves in the uniform grid. The lines with filled circles, open circles, filled diamonds, and open diamonds denote errors for slow, fast, Alfvén and entropy waves, respectively. The dashed lines indicate the relationship of errors in proportion to  $h^3$ , and that in proportion to  $h^2$ .

where  $\{U_{i,j}^m\} = \mathbf{U}_{i,j}$  denotes the conservative variables defined by equation (12) at the last stage,  $\{U_{i,j}^{m,0}\} = \mathbf{U}_{i,j}^0$  denotes that of the initial state, and  $\Delta S_{i,j} = \Delta x_{i,j} \Delta y_{i,j}$  denotes the cell surface. For the case of the AMR grids, only the cells of  $\ell = 1$  are taken into account for the sum in the region of  $x \leq 0.5$  since grid-levels of  $\ell = 0$  and 1 overlap in this region.

Figure 9 shows the  $L_1$  norm for regions of  $x \leq 0.5$  and  $x \geq 0.5$ , separately. The  $L_1$  norms of the uniform grid (dashed lines) in Figures 9a and 9b coincide with each other because of the symmetry. All the waves exhibit second-order accuracy for  $h_{\text{base}} \lesssim 1/64$ , and first-order accuracy for  $h_{\text{base}} \gtrsim 1/32$ , irrespective of the grid types and the wave modes, where  $h_{\text{base}}$  denotes the cell width of the coarsest grid (the base grid). This indicates that the numerical method basically has second-order accuracy, but the grids of  $h_{\text{base}} \gtrsim 1/32$  are too coarse to resolve the waves.

The AMR grids always exhibit smaller  $L_1$  norms than the uniform grids for given a wave mode and  $h_{\text{base}}$ . This is because the AMR grids resolve the waves using a grid in the region of  $x \leq 0.5$  that is two times finer than the corresponding uniform grids. This indicates that the AMR improves the solution of the wave propagation for all the wave. However, it should also be noted that the solution is improved more when the resolution of the uniform grid is increased by a factor two. Comparing the left and right sides for the AMR grids (Figs. 9a and 9b), the left region shows slightly smaller errors than the right region for the fast wave because the left side has finer resolution. In contrast, the left side has slightly larger errors than the right side for the slow and entropy waves, in spite of the finer resolution of the left side, indicating the effects of reflection of the waves at the boundaries between the fine and coarse grids. For the Alfvén wave, the significant dif-

ference is not observed between the left and right sides.

For the AMR grids, a wave propagates from the fine grid into the coarse grid at  $x = 0.5$ , and it also propagates from the coarse grid to the fine grid at  $x = 0$  and 1 via the periodic boundary condition. A significant reflection of the waves at  $x = 0.5$  is observed in the cases of very coarse grids ( $h_{\text{base}} \gtrsim 1/32$ ) in the  $v_y$  component of the fast wave and the  $v_x$  component of the slow wave. However, it should be noted that the amplitude of the components showing reflection is much smaller than that of the other components, e.g.,  $v_y$  has an amplitude of only 10 % of  $v_x$  for the fast wave.

Estimation of decay rate of waves is important for illustrating properties of a numerical method as indicated by Crockett et al. (2005), and we also estimate the decay rate for the test of the wave propagation on the uniform grids described above. The amplitude of the wave of the  $m$ -th mode is estimated by

$$w^m = \sum_{i,j} |l^m(\mathbf{U}_{i,j} - \mathbf{U}_0)| \quad (70)$$

where  $\mathbf{U}_{i,j}$  denotes the conservative variable,  $\mathbf{U}_0$  denotes that in the unperturbed state, and  $l^m$  denotes the left eigenvector of a wave mode evaluated in the unperturbed state. The superscript  $m$  indicates the modes of the MHD waves: the fast, slow, Alfvén, and entropy waves.

Figure 10 shows the decay rates for all the MHD waves as a function of the cell width. The decay rates for all the wave is almost in proportion to  $h^3$  for  $h \lesssim 1/64$  and  $h^2$  for  $h \gtrsim 1/64$ . This dependence of the decay rate on the cell width is consistent with Crockett et al. (2005), indicating that the region of the second-order accuracy exhibits the third-order accuracy in the decay rate. The third-order decay rate of the scheme presented here is also reported by Sugimoto et al. (2004) (see their Fig. 1), in which the same numerical flux presented here is adopted. In contrast, Ryu et al. (1995) reported a second-order decay rate by using a TVD scheme. The TVD approach is also adopted here but is based on the scheme of Fukuda & Hanawa (1999), where the MUSCL extrapolation is applied to the amplitude of the each eigenmode  $l^m \mathbf{U}$  rather than the primitive variables  $\mathbf{Q}$ .

## 8.2. Magnetic Flux Tube

The magnetic flux tube problem is proposed by Crockett et al. (2005), and is a test for stiffness of a MHD scheme. The model set-up is the same as that of Crockett et al. (2005). The unperturbed state is set as  $\rho = 1$ ,  $\mathbf{v} = 0$ ,  $B_x = 0$ , and  $B_z = 0$  in  $x, y \in [-0.5, 0.5]$ . The specific heat ratio is  $\gamma = 5/3$ . The computational domain is divided into a magnetized region of  $x \in [-0.2, 0.2]$  and non-magnetized regions. The magnetized region and the non-magnetized regions are balanced via the thermal pressure and magnetic pressure;  $B_y = \sqrt{80\pi}$  and  $P = 1$  in  $x \in [-0.2, 0.2]$ , and  $B_y = 0$  and  $P = 11$  in the remaining regions. The periodic boundary condition is imposed on the  $x = \pm 0.5$  and  $y = \pm 0.5$ . On this unperturbed state, the sinusoidal transverse velocity of  $v_x = \delta_{\text{pert}} c_A \sin(2\pi y)$  is imposed, and the amplitude of the velocity is set at  $\delta_{\text{pert}} = 0.01$ . This

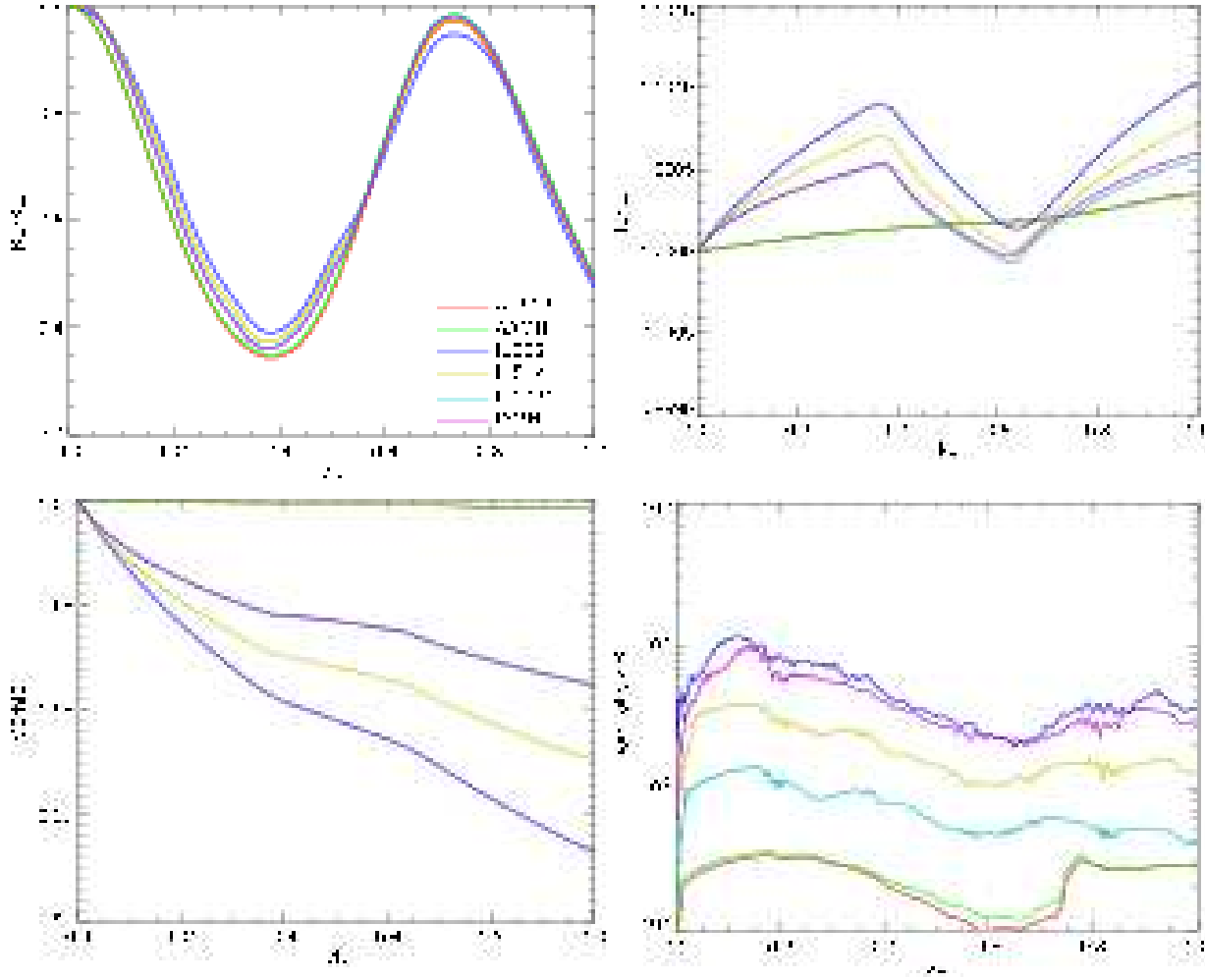


**Fig. 11.** Magnetic flux tube problem calculated by various models for (*top left*) kinetic energy, (*top right*) internal thermal energy, (*bottom left*) magnetic energy, and (*bottom right*)  $L_1$  norm of  $\nabla \cdot \mathbf{B}$ . The abscissa denotes the time normalized by Alfvén crossing time  $t_a = 1/c_A = 0.2236$ .

**Table 1.** Parameters for Magnetic Flux Tube

model	orientation	cell width ( $h$ )	grid
AU512	aligned	$1/512$	uniform
AAMR	aligned	$1/256 - 1/1024$	AMR ( $\ell_{\max} = 2$ )
IU256	inclined	$\sqrt{2}/256$	uniform
IU512	inclined	$\sqrt{2}/512$	uniform
IU1024	inclined	$\sqrt{2}/1024$	uniform
IAMR	inclined	$\sqrt{2}/256 - \sqrt{2}/1024$	AMR ( $\ell_{\max} = 2$ )

model is calculated using two types of grid: a uniform grid of  $h = 1/512$  (model AU512), and an AMR grid (model AAMR), as shown in Table 1. In the AMR grid, the maximum grid-level is set as  $\ell_{\max} = 2$ , and the following refinement criterion is adopted,

$$\max[\mathcal{E}(\rho_{i,j,k}), \mathcal{E}(P_{i,j,k})] \geq 10^{-1}, \quad (71)$$

$$\mathcal{E}(q_{i,j,k}) = \frac{|\partial_x^2 q_{i,j,k} + \partial_y^2 q_{i,j,k}| h^2}{q_{i,j,k}}. \quad (72)$$

This criterion captures the curvature of the density and pressure profiles, and the refinement is attributed mainly to the pressure jumps in this problem. Models with uniform grids are calculated until  $t = 6$  ( $= 26.83t_a$ ), and the models with the AMR grid are halted at  $t = 0.2236$  ( $= t_a$ ) because of computational cost, where  $t_a = 1/c_A = 1/\sqrt{20}$  denotes Alfvén crossing time.

Grid-inclined flux tube models are also examined. The model set-up is the same as that of the grid-aligned model

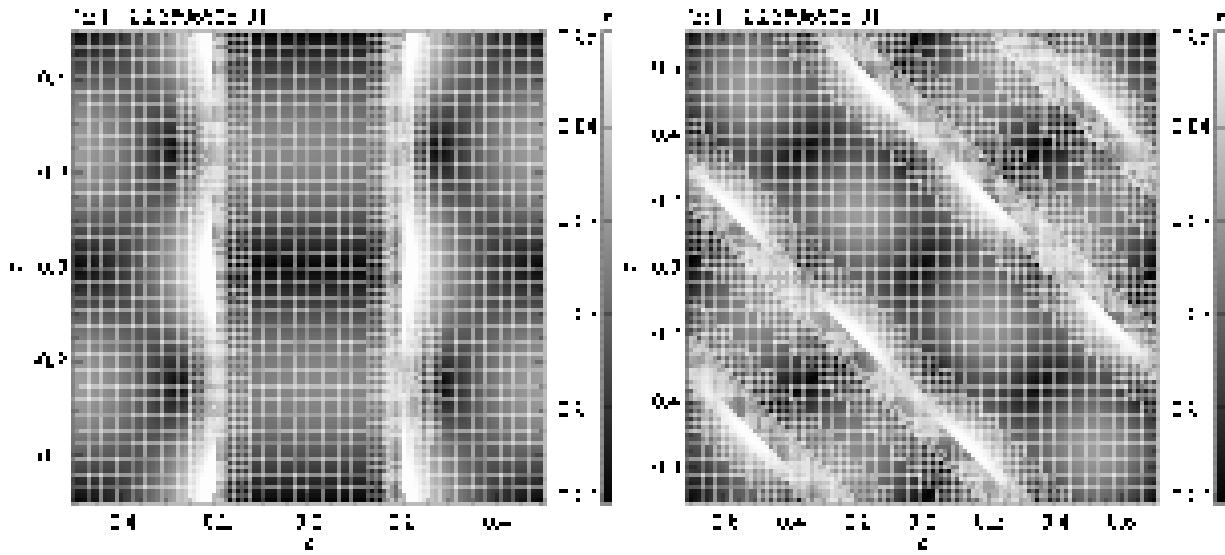


Fig. 12. Magnetic flux tube for models (a) AAMR and (b) IAMR. at the stage of  $t/t_a = 1$ . The gray scales denote the velocity  $|v|$ , and the white rectangles denote the block distributions. (a) The region of  $x \in [-0.2, 0.2]$  is magnetized, and (b) the diagonal region is non-magnetized. The boundaries between the magnetic and non-magnetic regions are resolved by the fine blocks.

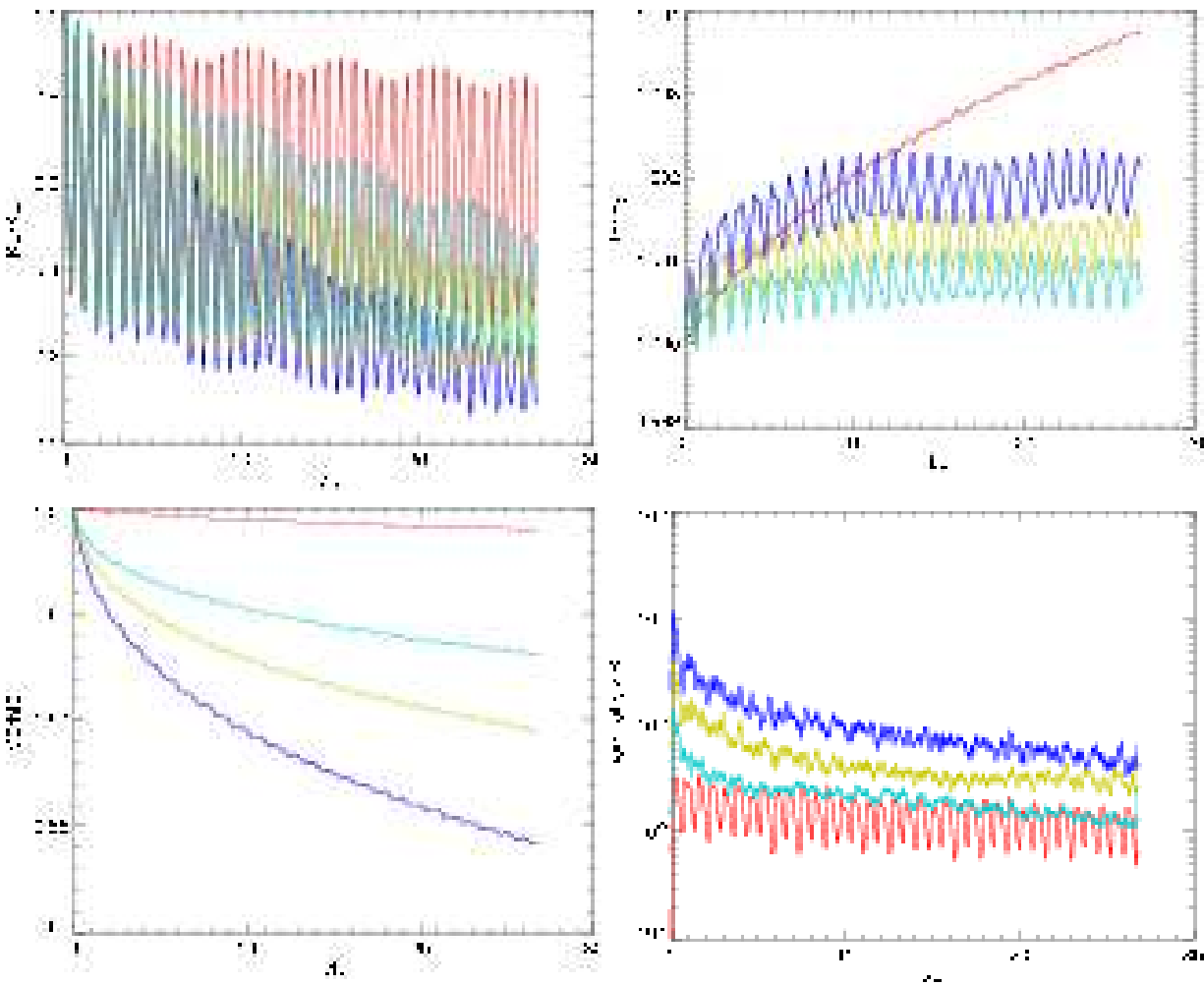


Fig. 13. Magnetic flux tube problem calculated by the uniform grid models for (top left) kinetic energy, (top right) internal energy, (bottom left) magnetic energy, and (bottom right)  $L_1$  norm of  $\nabla \cdot \mathbf{B}$ . The color legend is same as that of Figure 11.

described above, but the coordinates are rotated at an angle of  $45^\circ$ . Because of this rotation, the computational box is larger than the grid-aligned model by a factor  $\sqrt{2}$ :  $x, y \in [1/\sqrt{2}, -1/\sqrt{2}]$ . We introduce a taper region at the boundaries between the magnetic and non-magnetic regions, in order to reduce the initial  $\nabla \cdot \mathbf{B}$  error. At the taper region, the pressure and magnetic field have a tanh profile, the scale length of which is twice the cell width. For the inclined cases, four models are constructed as shown in Table 1; three models are calculated using a uniform grid by changing the resolution from  $h = \sqrt{2}/256$  to  $\sqrt{2}/1024$  (models IU256, IU512, and IU1024), and one using the AMR grid (model IAMR).

Figure 11 shows the kinetic energy, internal thermal energy, magnetic energy, and  $L_1$  norm of  $\nabla \cdot \mathbf{B}$  error as a function of time for  $0 \leq t \leq t_a$ . The three former energies are normalized using the initial values in the plots. The divergence error is calculated as follows (see the ninth component of equations [12]–[14]):

$$(\nabla \cdot \mathbf{B})_{i,j,k}^{n+1/2} = \frac{\psi_{i,j,k}^n - \psi_{i,j,k}^{n+1} e^{\Delta t c_h^2 / c_p^2}}{c_h^2 \Delta t}. \quad (73)$$

In the period  $0 \leq t \leq t_a$ , all the models are calculated without any indications of the instability. The two grid-aligned models (AU512 and AAMR) exhibit good agreement with each other, and  $L_1$  norms of the  $\nabla \cdot \mathbf{B}$  are remain low. The block distribution of the AMR models is shown in Figure 12a, and the fine blocks cover the boundaries between the magnetic and non-magnetic regions. For the grid-inclined models, the three models (IU256, IU512, and IU1024) are calculated with uniform grids of different resolutions, and these models show approximately first-order convergence ( $\propto h^{1.18}$ ). The model with the AMR grid (IAMR) shows an evolution very similar to the model with the finest uniform grid (IU1024), as shown in Figure 11. For model IAMR, the boundaries between the magnetic and non-magnetic regions are resolved by the finest blocks whose cell width is the same as that of model IU1024 (Fig. 12b). This implies that a dominant error is caused in the boundary between the magnetic and non-magnetic regions. However, model IAMR has a  $\nabla \cdot \mathbf{B}$  error as large as that of model IU246, which has the same resolution as the coarsest grid-level of model IAMR. Examining the velocity distributions shown in Figure 12, model AAMR exhibits good agreement with IAMR when it rotates at angle of  $45^\circ$ ; note that the diagonal region of Figure 12b corresponds to regions of  $x \leq -0.2$  and  $x \geq 0.2$  in Figure 12a.

Figure 13 is the same as Figure 11 except for  $0 \leq t \leq 6$  and the uniform grid models. The long time calculations are performed successfully without any instabilities for all the uniform grid models. The kinetic energy of the grid-aligned model (AU512) decays slightly. For the grid-inclined models, the model with higher resolution shows less decay in the kinetic energy, but the kinetic energies of the finest grid-inclined model (IU1024) is about half those of the grid-aligned model (AU512) at the peak of the final osculation. The internal energies show different tenden-

cies in the grid-aligned and -inclined models, but their gradual increases are within the order of 0.1%. The  $L_1$  norms of the  $\nabla \cdot \mathbf{B}$  remain low in the grid-aligned model (model AU512) and the grid-aligned model with the fine grid (model IU1024).

### 8.3. Double Mach Reflection

We consider the double Mach reflection problem as a hydrodynamics test problem. This test problem was initially proposed by Woodward & Colella (1984), and has since been widely used for testing high resolution schemes. A planar shock of Mach 10 travels in a medium of  $\rho = 1.4$ ,  $P = 1$ , and  $\gamma = 1.4$  with incident angle of  $60^\circ$  against a rigid wall. The incident shock interacts with the wall, and a complicated structure develops featuring a strong and weak reflected shock, contact discontinuities, and a small jet at the wall (lower boundary;  $1/6 \leq x \leq 4$  and  $y = 0$ ). The computational domain given by  $x \in [0, 4]$  and  $y \in [0, 1]$  is covered by  $32 \times 8$  blocks at  $\ell = 0$ , and the maximum grid-level is set at  $\ell_{\max} = 4$ . Each grid has  $8^2$  cells ( $N_x = N_y = 8$ ), and so the minimum and maximum resolutions are  $h = 1/64$  and  $1/1024$ , respectively. The following refinement criterion is adopted,

$$\max[\mathcal{E}(\rho_{i,j,k}), \mathcal{E}(P_{i,j,k})] \geq 10^{-2}, \quad (74)$$

where  $\mathcal{E}$  is defined by equation (72). Three-dimensional code is applied to this problem even though it has a two-dimensional symmetry, with all the variables kept constant in the  $z$ -direction. In order to maintain this two-dimensional symmetry, the condition  $\mathbf{F}_z = 0$  is imposed. The Roe scheme is modified here based on Kim et al. (2003) in order to avoid the carbuncle instability at shock waves. The carbuncle instability refers to a protuberant shock profile, which is an unphysical phenomenon and mashes up shock waves (see, e.g., Perry & Imlay 1988). This is thought to be attributed to a low numerical diffusion of the Roe's scheme, and calculations having high resolutions tend to suffer from this instability.

Figure 14a shows the density distribution at  $t = 0.2$ . The shock waves are resolved by finest grids as shown in Figure 14b. Figure 14c shows an enlargement of Figure 14a around the double Mach stems. An eddy is clearly resolved at the end of the jet, and it can be seen even more clearly in the entropy distribution  $P/\rho^\gamma$  (Fig. 14d). The shock wave is resolved clearly at  $x = 2.8$  because the carbuncle instability was eliminated. Without eliminating the carbuncle instability, a serious instability was observed in this shock wave, and the eddy was also mashed up. At  $(x, y) = (2.3, 0.1)$ , the discontinuity of the shear begins to twist, and another eddy may develop as shown by Shi et al. (2003).

The double Mach reflection problem is also calculated using uniform grids changing the resolution from  $h = 1/64$  to  $1/1024$  in order to confirm the convergence. This test exhibits an order of convergence of 1.23, which is slightly higher than the first order, in spite of implementing the second order accuracy. This may be because the slope limiter in the MUSCL extrapolations reduces the accuracy to the first order in the regions having shock waves and



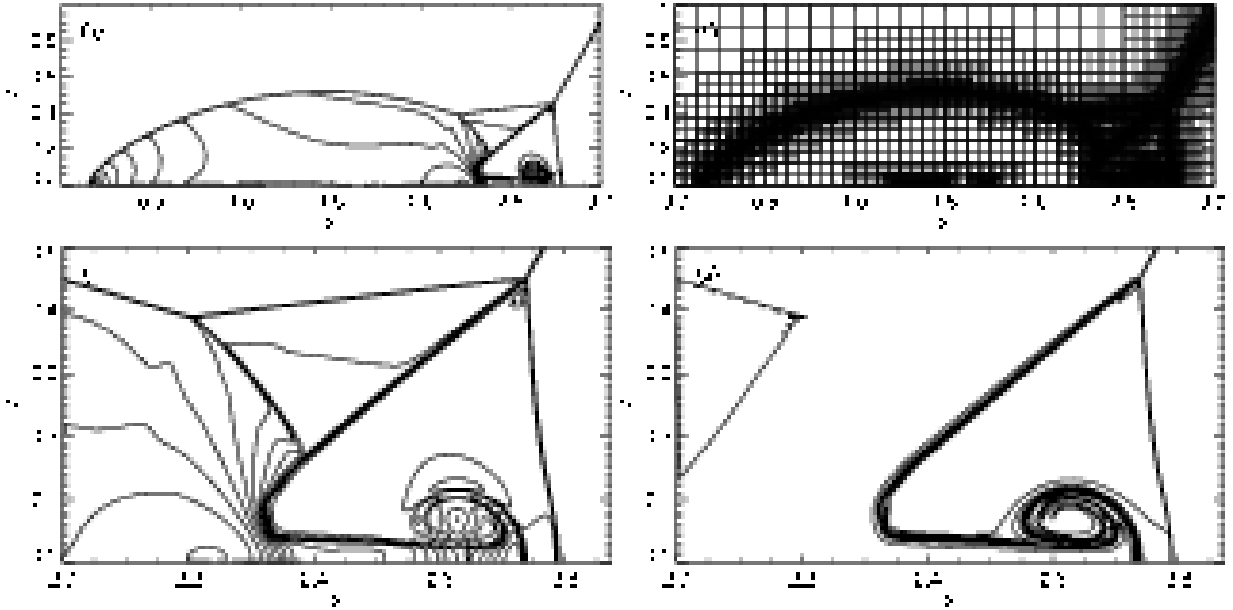


**Fig. 14.** Double Mach reflection problem at  $t = 0.2$ , (a) density distribution in  $[0, 3] \times [0, 1]$ , (b) block distribution in  $[0, 3] \times [0, 1]$ , (c) enlargement of Figure 14a ( $[2, 2.9] \times [0, 0.5]$ ), and (d) distribution of  $P/\rho^\gamma$ . In (a) and (c) 30 contour lines are shown in the range  $1.5 \leq \rho \leq 22.9705$ , while in (d) 22 contour lines are shown in the range  $1.0 \leq P/\rho^\gamma \leq 11.5$ .

contact discontinuities.

#### 8.4. MHD Rotor Problem

The MHD rotor problem was first proposed by Balsara & Spicer (1999), and it tests the propagation of non-linear Alfvén waves. The model set-up is in the same manner as that of Tóth (2000) and Crockett et al. (2005). The computational domain is a unit square of  $x, y \in [0, 1]$ . In the initial stage, a uniform cylinder with  $\rho = 10$ ,  $P = 1$ , and radius 0.1 rotates at an angular velocity of 20. The ambient medium is at rest with  $\rho = 1$ ,  $P = 1$ , and  $\mathbf{v} = 0$ . At the boundary between the cylinder and ambient medium, a taper region is used in order to reduce the initial transition (see Tóth 2000). The computational domain is subject to a uniform magnetic field,  $(B_x, B_y, B_z) = (5, 0, 0)$ . The adiabatic index of the gas is  $\gamma = 1.4$ . The computational domain is covered by  $16 \times 16$  blocks at  $\ell = 0$ , and each block consists of  $8 \times 8$  cells ( $N_x = N_y = 8$ ). The maximum grid-level is set at  $\ell_{\max} = 2$ . The coarsest and finest grids therefore exhibit an effective resolution of  $h = 1/128$  and  $1/512$ , respectively. The following refinement criterion is adopted,

$$\max[\mathcal{E}(\rho_{i,j,k}), \mathcal{E}(P_{i,j,k})] \geq 1, \quad (75)$$

$$\mathcal{E}(q_{i,j,k}) = [\mathcal{E}_x^2(q_{i,j,k}) + \mathcal{E}_y^2(q_{i,j,k}) + \mathcal{E}_z^2(q_{i,j,k})]^{1/2}, \quad (76)$$

$$\mathcal{E}_x(q_{i,j,k}) = \frac{h^2 \partial_x^2 q_{i,j,k}}{h |\partial_x q_{i+1/2,j,k}| + h |\partial_x q_{i-1/2,j,k}| + \epsilon h^2 \partial_x^2 q_{i,j,k}}, \quad (77)$$

and  $\mathcal{E}_y$  and  $\mathcal{E}_z$  are defined in a similar manner to  $\mathcal{E}_x$ , where  $\epsilon = 10^{-2}$  (e.g., Fryxell et al. 2000).

Figures 15a-15d show the density, thermal pressure, Mach number, magnetic pressure at  $t = 0.15$ . The finest

grids capture the outer shock fronts and inner complex structures, as shown in Figure 15f. The distribution of the physical variables plotted here exhibit excellent agreement with Figure 18 of Tóth (2000) and Figure 12 of Crockett et al. (2005). Figure 15e shows the amplitude of the magnetic divergence error normalized by the cell width and the local magnetic field strength,  $h(\nabla \cdot \mathbf{B})/|\mathbf{B}|$ , where  $\nabla \cdot \mathbf{B}$  is estimated using equation (73). The divergence error reaches a maximum value of  $1.5 \times 10^{-2}$  at the inner discontinuity, and is  $2 \times 10^{-3}$  at the outer shock fronts. The divergence cleaning of Dedner et al. (2002) keeps the divergence error small.

#### 8.5. Accuracy of Multigrid Method

The accuracy of the multigrid method is examined using the approach of Matsumoto & Hanawa (2003a). Two uniform spheres of masses 1 and 2, both having a radius of  $6/1024$ , are located at  $(x, y, z) = (12/1024, 0, 0)$  and  $(-12/1024, 0, 0)$  in the computational domain  $x, y, z \in [-0.5, 0.5]$ . A Dirichlet physical boundary condition is imposed on  $\Phi$ , and it is evaluated by the multi-pole expansion of the density distribution at  $\ell = 0$ , where the monopole, dipole, and quadruple moments are taken into account.

The computation was started from the initial guess  $\Phi = 0$ . The residual decreased by more than a factor of several hundred with each FMG iteration given by equations (59) and (60). After 10 iterations, the residual was of the order of the round-off error. The numerical solution for the gravity obtained by this computation is compared to the exact analytic solution.

Figure 16 shows the relative error of the numerically calculated gravity,  $|\mathbf{g} - \mathbf{g}_{\text{ex}}|/|\mathbf{g}_{\text{ex}}|$ , on a logarithmic scale, where  $\mathbf{g}_{\text{ex}}$  denotes the exact gravity obtained analytically.

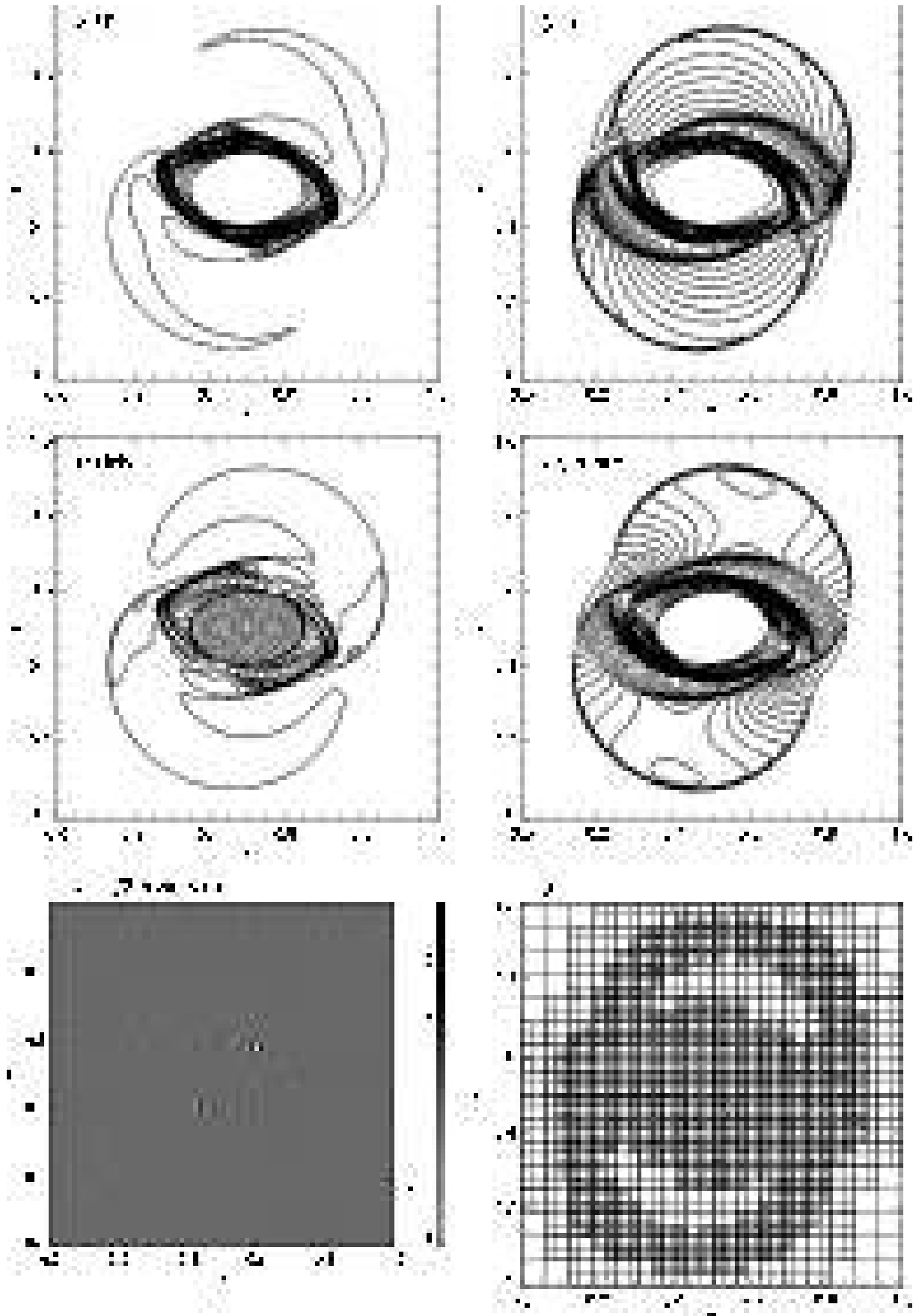


**Fig. 15.** MHD rotor problem solved by the AMR code. (a) Density, (b) thermal pressure, (c) Mach number, (d) magnetic pressure, (e) magnetic monopole, and (f) grid distribution are shown at  $t = 0.15$ . In (a)-(d) 30 contour lines are shown in the ranges of  $0.483 \leq \rho \leq 12.95$ ,  $0.0202 \leq P \leq 2.008$ ,  $0 \leq |\mathbf{v}|/c_s \leq 8.18$ , and  $0.0177 \leq \mathbf{B}^2/8\pi \leq 2.642$ , respectively.

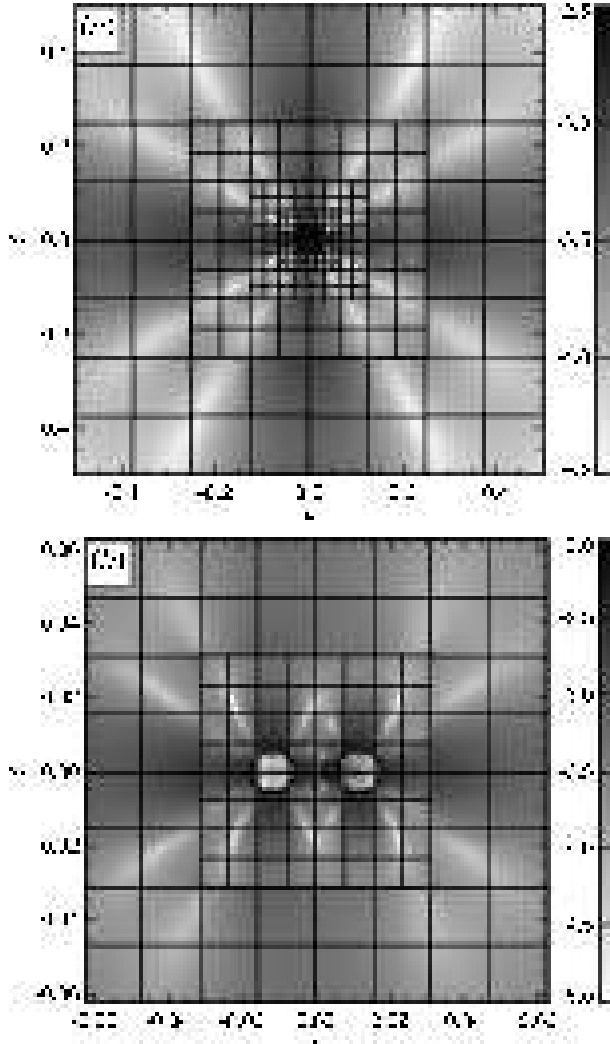


**Fig. 16.** Distribution of the relative error of the numerically calculated gravity in the  $z=0$  plane with  $N_x = N_y = N_z = 16$  after 10 iterations of the FMG-cycles. The gray scale denotes  $\log(|\mathbf{g} - \mathbf{g}_{\text{ex}}|/|\mathbf{g}_{\text{ex}}|)$ , and the rectangles indicate the block distribution. Panel *b* is an enlargement of panel *a*.

In this calculation,  $N_x = N_y = N_z = 16$  and  $\ell_{\text{max}} = 4$  are adopted. The block distribution is also shown in Figure 16. The maximum error occurs at the edges of the spheres due to the discretization error that arises from the sharp density contrast of the spheres. In the other domains, the error is less than  $\sim 10^{-3}$ . It is noteworthy that no significant error appears at the interfaces between the coarse and fine grids. This is attributed to the refluxing of the gravity described in § 6.2.

Figure 17 shows the dependence of the error on resolution. The error of the gravity is measured by changing the number of cells inside a block,  $N_x$ ,  $N_y$ , and  $N_z$ , but fixing the block distribution. The ordinates of Figures 17*a*, 17*b*, and 17*c* denote the errors measured by the average, root mean square, and maximum values, corresponding to the  $L_1$ ,  $L_2$ , and  $L_\infty$  norms, respectively. The abscissa denotes the cell width of the coarsest grid  $\ell = 0$ . The five lines show the errors at the grid-levels of  $\ell = 0, \dots, 4$ ,

while the five points in the lines denote the errors for  $N_x = N_y = N_z = 2, 4, 8, 16$ , and  $32$ . All the lines, except for  $\ell = 4$  in Figure 17*c*, exhibit second-order accuracy for the multigrid method presented here. By contrast, the line of  $\ell = 4$  in Figure 17*c* shows a first-order accuracy. This is attributed to the discretization error of the density imposed on this grid-level.

### 8.6. Convergence of Multigrid Method

The reduction of the residual defined by equation (50), is measured to evaluate the efficiency of the iteration for the same problem as described in § 8.5. Figure 18 shows the maximum residual in each grid-level as a function of the number of the FMG-cycles defined by equations (59) and (60) for the cases  $N_x = N_y = N_z = 8, 16$ , and  $32$ . The residuals plotted here are multiplied by  $h^2$  so that they have a dimension of  $\Psi$ . For the case  $N_x = N_y = N_z = 8$  (Fig. 18*a*), the residuals in all the grid-levels decrease in proportion to  $\exp(-6n)$ . After 7 iterations of the FMG-cycles, the residuals at all grid-levels reach the round-off error. On the other hand, for the cases  $N_x = N_y = N_z = 16$  and  $32$  (Figs. 18*b* and 18*c*), the rate at which the residuals decrease on the coarse grid-levels are slower than those of the fine grid-levels. The slower convergence is due to the boundary condition imposed on the coarsest grid.

### 8.7. Collapse and Fragmentation of an Isothermal Cloud

The present numerical technique is applied to the problem of the collapse and fragmentation of an isothermal cloud as a gravitational hydrodynamics test problem. While isothermal collapse has been calculated by many authors, the particular model given in Bate & Burkert (1997) and Truelove et al. (1998) is followed here. The initial cloud has a uniform, spherical density distribution, and rotates rigidly around the  $z$ -axis. The mass of the cloud is  $1M_\odot$ , and the radius is  $R_c = 5 \times 10^{16}$  cm, and so the density of the cloud is therefore  $\rho_0 = 3.79 \times 10^{-18}$  g cm $^{-3}$ . Conventionally, a cloud is characterized by two global quantities,  $\alpha = E_{\text{th}}/|E_{\text{grav}}|$  and  $\beta = E_{\text{rot}}/|E_{\text{grav}}|$ , where  $E_{\text{th}}$ ,  $E_{\text{rot}}$ , and  $E_{\text{grav}}$  denote the thermal, rotation, and gravitational energies. The cloud here has  $\alpha = 0.26$  and  $\beta = 0.16$ . The sound speed and the angular velocity are obtained as  $c_s = 0.166$  km s $^{-1}$  and  $\Omega = 7.14 \times 10^{-13}$  s $^{-1}$ , respectively. The cloud is perturbed by a bar perturbation with an amplitude of 10%;  $\rho = \rho_0(1 + 0.1 \cos 2\phi)$ . The cloud is embedded in an ambient gas, whose density is  $0.01\rho_0$ .

The computational domain is  $x, y, z \in [-2R_c, 2R_c] \times [-2R_c, 2R_c] \times [0, 2R_c]$ , and a mirror boundary condition is imposed on the  $z=0$  plane. Blocks of  $N_x = N_y = N_z = 8$  are adopted. At the initial stage,  $16 \times 16 \times 8$  blocks are distributed at the grid-level of  $\ell = 0$ . The cloud radius  $R_c$  is therefore resolved by 32 cells. This initial resolution is same as that of Truelove et al. (1998). The Jeans condition is employed as a refinement criterion; the blocks are refined when the Jeans length is shorter than 8 times of cell width;  $(\pi c_s^2 / G\rho)^{1/2} < 8h$ . This refinement criterion is twice as severe as that of Truelove et al. (1997).

Figure 19 shows the maximum density as a function of

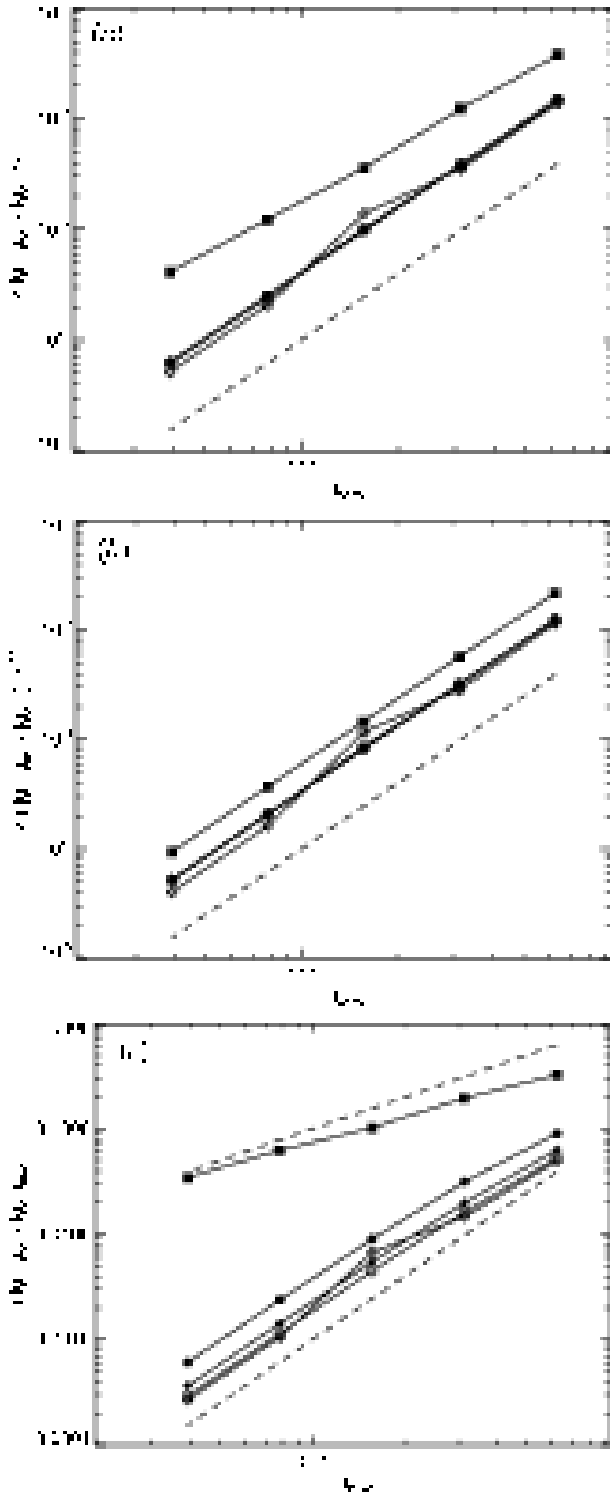


Fig. 17. The relative error of the numerically computed gravity  $|g - g_{\text{ex}}| / |g_{\text{ex}}|$  as a function of  $h_{\text{base}}$  (cell width of the coarsest grids). The error is measured by (a) average, (b) root mean square, and (c) maximum on each grid-level separately. The open diamonds, open circles, filled diamonds, filled circles, and filled square denote the errors on grids of  $\ell = 0, 1, 2, 3$ , and 4, respectively. The dashed lines indicate the relationship of (a-c) errors in proportion to  $h_{\text{base}}^2$ , and (c) those in proportion to  $h_{\text{base}}$ .

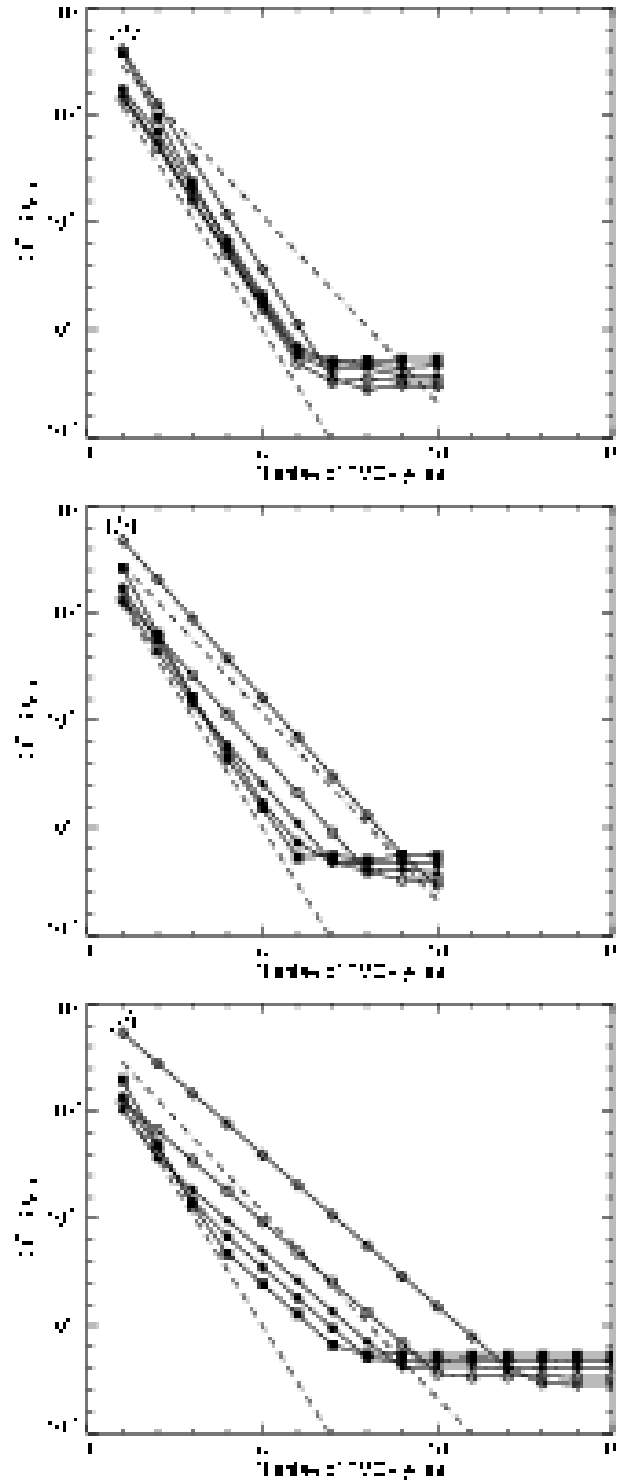


Fig. 18. The maximum residual ( $|h^2 R|_{\text{max}}$ ) as a function of the number of the FMG-cycles for the cases (a)  $N_x = N_y = N_z = 8$ , (b)  $N_x = N_y = N_z = 16$ , and (c)  $N_x = N_y = N_z = 32$ . The open diamonds, open circles, filled diamonds, filled circles, and filled square denote the residuals measured on grids of  $\ell = 0, 1, 2, 3$ , and 4, respectively. The dashed line displays the relationships  $|h^2 R^n|_{\text{max}} \propto \exp(-4n)$  and  $\exp(-6n)$ , where  $n$  denotes the number of the FMG-cycles.

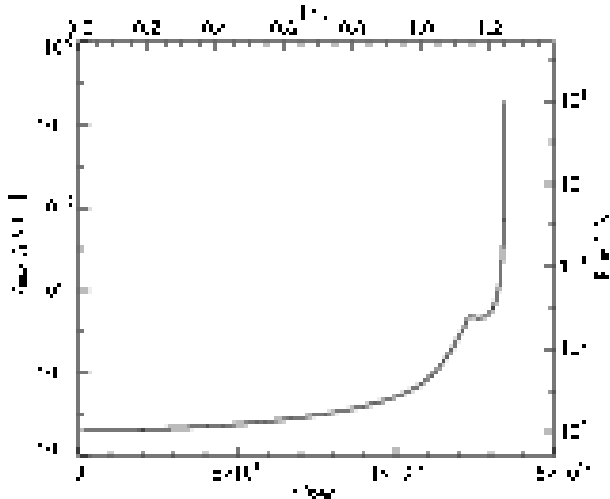


Fig. 19. Maximum density as a function of time for the problem of the collapse and fragmentation of an isothermal cloud.

time. The central density initially increases gradually as the cloud collapses. A thin disk forms due to the fast rotation of the cloud when the central density reaches a value of around  $\rho_{\max} = 2 \times 10^{-15} \text{ g cm}^{-3}$  at  $t = 1.25 \times 10^{12} \text{ s}$  ( $= 1.16 t_{\text{ff}}$ ), where  $t_{\text{ff}} = (3\pi/32G\rho_0)^{1/2} = 5.60 \times 10^{12} \text{ s}$ , and this disk bounces in the  $z$ -direction. After the bounce, the density increases more rapidly, and approaches a singularity at  $t = 1.35 \times 10^{12} \text{ s}$  ( $= 1.25 t_{\text{ff}}$ ).

Figure 20a shows the density distribution in the  $z = 0$  plane when  $\rho_{\max} = 1.02 \times 10^5 \rho_0$ . The disk has two density peaks, which are resolved by the fine blocks. Each density peak has a filamentary structure. This density structure was also found by Truelove et al. (1998) (see their Fig. 12).

Figure 20b shows the upper left bar when  $\rho_{\max} = 1.01 \times 10^8 \rho_0$ . The bar collapses to form a very narrow filament. This is also consistent with Truelove et al. (1998) (see their Fig. 13).

### 8.8. Collapse and Outflow Formation of a Cloud Core with Slow Rotation and Oblique Magnetic Field

The collapse of a cloud with magnetic field parallel to the rotation axis has been simulated by Machida et al. (2004); Machida et al. (2005a); Machida et al. (2005b); Ziegler (2005); Banerjee & Pudritz (2006); Fromang et al. (2006), while the collapse of an oblique magnetic field has been simulated by Matsumoto & Tomisaka (2004); Machida et al. (2006). In the case of an oblique magnetic field, the rotation axis changes its direction due to the anisotropic magnetic braking during the collapse, and an outflow is ejected after an adiabatic core formation.

In this paper, the model MF45 of Matsumoto & Tomisaka (2004) was calculated using the AMR presented here. The initial cloud has the density profile of a critical Bonnor-Ebert sphere (Ebert 1955; Bonnor 1956), but the density is increased by a factor of 1.68. The central density is  $\rho_0 = 1 \times 10^{-19} \text{ g cm}^{-3}$ , and the radius of the cloud is  $R_c = 5.49 \times 10^{17} \text{ cm}$ . The cloud rotates slowly at an an-

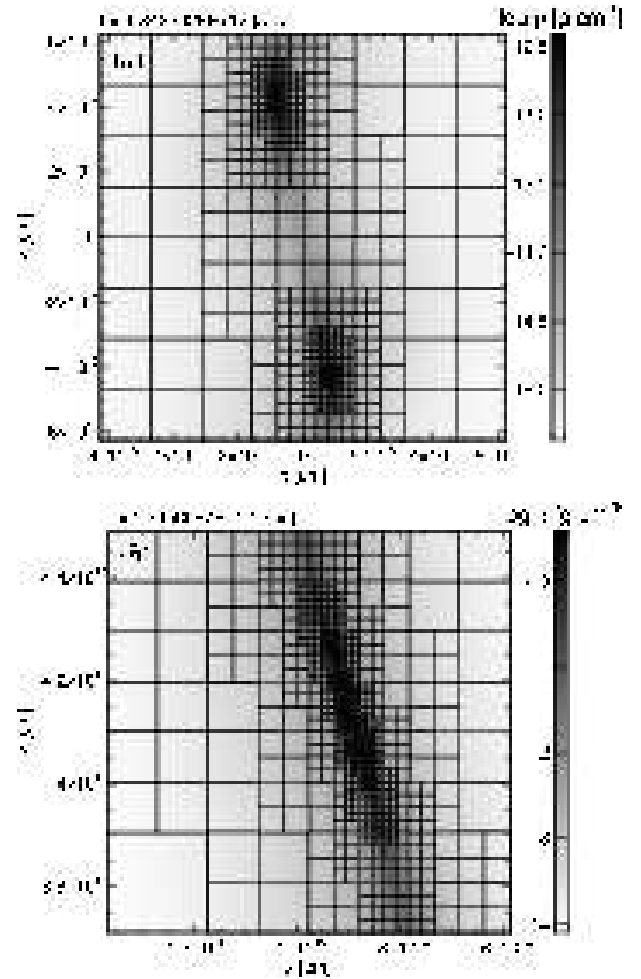
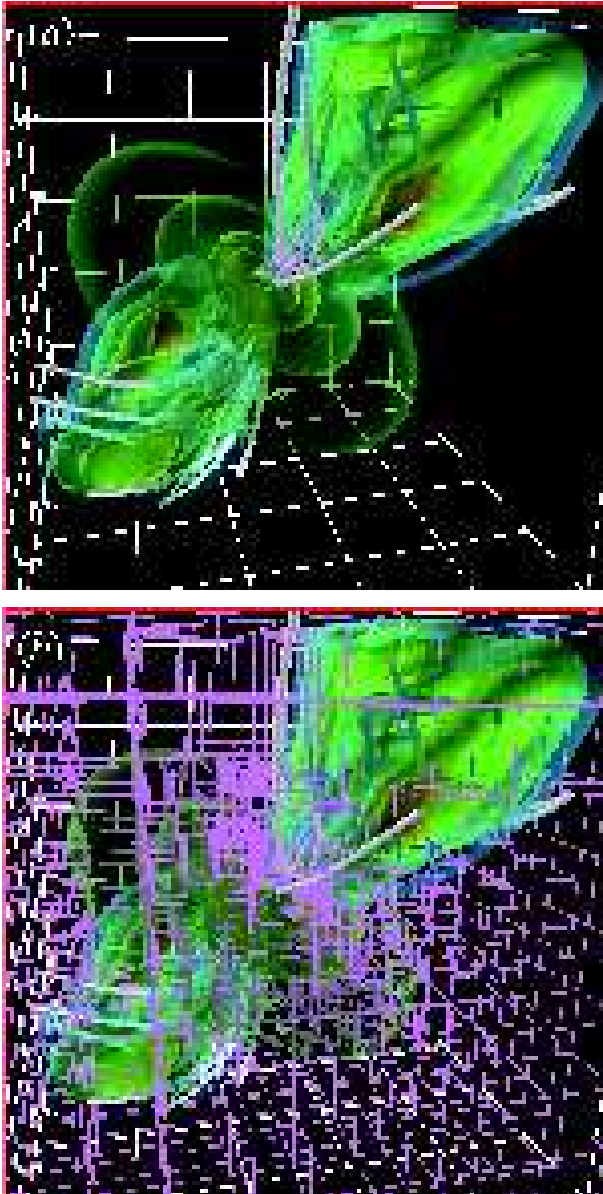


Fig. 20. Collapse and fragmentation of a rotating isothermal cloud. The gray scale denotes logarithmic density in the  $z = 0$  plane, and the rectangles indicate the block distribution. (a) The central region of the cloud when  $\rho_{\max} = 1.02 \times 10^5 \rho_0$  on the grid-levels  $\ell = 3 - 7$ . (b) Enlargement around the upper left fragment when  $\rho_{\max} = 1.01 \times 10^8 \rho_0$  on grid-levels  $\ell = 6 - 12$ .

gular velocity of  $\Omega_0 = 7.11 \times 10^{-7} \text{ yr}^{-1}$  ( $= 0.15 t_{\text{ff}}^{-1}$ ), where the freefall time is  $t_{\text{ff}} = 2.10 \times 10^5 \text{ yr}$ . The initial magnetic field is inclined at an angle of  $45^\circ$  with respect to the  $z$ -axis (rotation axis), and has a strength  $18.6 \mu\text{G}$ . The cloud has parameters given by  $\alpha = 0.5$ ,  $\beta = 0.02$ , and  $E_{\text{mag}}/|E_{\text{grav}}| = 0.721$ , where  $E_{\text{mag}}$  denotes the total magnetic energy inside the cloud.

In order to mimic the formation of the first stellar core, the equation of state is changed according to the density: an isothermal gas of  $T = 10 \text{ K}$  ( $c_s = 0.19 \text{ km s}^{-1}$ ) is assumed when density is less than  $\rho_{\text{cr}} = 2 \times 10^{-13} \text{ g cm}^{-3}$ , while a polytrope gas of  $\gamma = 5/3$  is assumed when density is higher than  $\rho_{\text{cr}}$ .

Figure 21a shows the central region of  $(287 \text{ AU})^3$  at  $t = 4.81 \times 10^5 \text{ yr}$ . As calculated by Matsumoto & Tomisaka (2004), the outflow is ejected from the region near the first core. The outflow speed reaches  $10c_s$ , which is also consistent with a previous calculation.



**Fig. 21.** (a) Three-dimensional view of protostellar collapse and outflow formation at  $t = 4.81 \times 10^5$  yr. The 6 disk-shaped isosurfaces are shown for  $4.7 \leq \log \rho / \rho_0 \leq 7.0$ , and the 4 bipolar isosurfaces are shown for  $2.0 \leq v_r / c_s \leq 9.0$ . The tubes indicate the magnetic field lines. The coordinates are shown in the units of  $c_s / (4\pi G \rho_0)^{1/2}$ . (b) Same as panel a but the block distribution is overlaid. The grid-levels is ranged from 11 to 13.

Figure 21b shows the block distribution, where grid-levels of  $\ell = 11 - 13$  are shown. Each grid-level has  $8^3$  blocks. This grid distribution reproduces effectively the same cell distribution as a nested grid including  $64^3$  cells in each grid-level.

## 9. Summary

SFUMATO, a self-gravitational MHD code applying the AMR technique is presented. The grid is configured

in a block structure.

The MHD scheme is implemented so that it is of second-order spatial accuracy by means of the TVD approach. The upwind numerical flux is obtained by the linearized Riemann solver. The scheme is fully cell-centered, and the divergence error of the magnetic fields is cleaned. The convergence tests of the linearized MHD waves exhibit a second-order accuracy, and the decay rates shows a third-order accuracy. Stiffness of the scheme is confirmed by the MHD flux tube problems.

The self-gravity is solved by a multigrid method composed of: (1) a FMG-cycle on the AMR hierarchical grids, (2) a V-cycle on these grids, and (3) a FMG-cycle on the base grid. The FMG-cycle on the AMR hierarchical grids enables a scalable dependence on the number of cells. The multigrid method ensures that the solution converges rapidly; the residual is reduced by a factor of  $10^{-3} - 10^{-2}$  every iteration. The multigrid method exhibits a second-order spatial accuracy. Moreover, no spurious features appear at the interfaces between fine and coarse grid-levels, due to the flux conservation at the interface.

The MHD scheme and multigrid method are combined so as to have second-order temporal accuracy. The time-marching has two modes: synchronous and adaptive time-step modes. The former mode is adopted for problems including self-gravity, while the latter mode is used for all other problems.

The AMR code was tested by considering test problems given by double Mach reflection, the MHD rotor, fragmentation of an isothermal cloud, and outflow formation in a collapsing cloud. The present results are in good agreement with those of previous studies conducted by the present author as well as other authors.

The author would like to thank K. Tomisaka and T. Hanawa for valuable discussions. The author thanks the anonymous referee for his/her valuable comments, which have been very helpful in improving the paper. Numerical computations were carried out on VPP5000 at the Center for Computational Astrophysics, CfCA, of the National Astronomical Observatory of Japan, and SX6 at Japan Aerospace Exploration Agency, JAXA. This research was supported in part by the Hosei Society of Humanity and Environment, and by Grants-in-Aid for Young Scientists (B) 16740115, 18740113, for Scientific Research (C) 17540212, and for Scientific Research (B) 17340059 awarded by the Ministry of Education, Culture, Sports, Science and Technology, Japan.

## References

- Shi, J., Zhang, Y.-T. & Shu, C.-W. 2003, *Journal of Computational Physics*, 186, 690
- Balsara, D. S., & Kim, J. 2004, *ApJ*, 602, 1079
- Balsara, D. S., & Spicer, D. S. 1999, *Journal of Computational Physics*, 149, 270
- Balsara, D. S. 2001, *Journal of Computational Physics*, 174, 614
- Banerjee, R., & Pudritz, R. E. 2006, *ApJ*, 641, 949
- Bate, M. R., & Burkert, A. 1997, *MNRAS*, 288, 1060

- Berger, M. J., & Colella, P. 1989, *Journal of Computational Physics*, 82, 64
- Berger, M. J., & Olinger, J. 1984, *Journal of Computational Physics*, 83, 484
- Bonnor, W. B. 1956, *MNRAS*, 116,351
- Crockett, R. K., Colella, P., Fisher, R. T., Klein, R. I., & McKee, C. F. 2005, *Journal of Computational Physics*, 203, 422
- Dedner, A., Kemm, F., Kröner, D., Munz, C.-D., Schnitzer, T., & Wesenberg, M. 2002, *Journal of Computational Physics*, 175, 645
- Ebert, R. 1955, *Z. Astrophys.*, 37, 222
- Fromang, S., Hennebelle, P., & Teyssier, R. 2006, *ArXiv Astrophysics e-prints*, arXiv:astro-ph/0607230
- Fryxell, B., et al. 2000, *ApJS*, 131, 273
- Fukuda, N., & Hanawa, T. 1999, *ApJ*, 517, 226
- Gardiner, T. A., & Stone, J. M. 2005, *Journal of Computational Physics*, 205, 509
- Hirsch, C. 1990, *Numerical Computation, of Internal and External Flows*, Vol. 2 (Chichester: Wiley)
- Kim, S., Kim, C., Rho, O., & Hong, S. K. 2003, *Journal of Computational Physics*, 185, 342
- Klein, R. I., Inutsuka, S.-i., Padoan, P., & Tomisaka, K. 2006, *ArXiv Astrophysics e-prints*, arXiv:astro-ph/0603711
- Machida, M. N., Tomisaka, K., & Matsumoto, T. 2004, *MNRAS*, 348, L1
- Machida, M. N., Matsumoto, T., Tomisaka, K., & Hanawa, T. 2005, *MNRAS*, 362, 369
- Machida, M. N., Matsumoto, T., Hanawa, T., & Tomisaka, K. 2005, *MNRAS*, 362, 382
- Machida, M. N., Matsumoto, T., Hanawa, T., & Tomisaka, K. 2006, *ApJ*, 645, 1227
- Matsumoto, T., & Hanawa, T. 2003, *ApJ*, 583, 296
- Matsumoto, T., & Hanawa, T. 2003, *ApJ*, 595, 913
- Matsumoto, T., & Tomisaka, K. 2004, *ApJ*, 616, 266
- Matsumoto, T., Machida, M. N., Tomisaka, K., & Hanawa, T. 2004, *Computer Physics Communications*, 164, 229
- Norman, M. L., & Bryan, G. L. 1999, *ASSL Vol. 240: Numerical Astrophysics*, 19
- Peery, K.M., & Imlay, S.T. 1988, *AIAA Paper 88-2904*
- Press, W. H., & Teukolsky, S. A. 1991, *Computers in Physics*, 5, 514
- Roe, P. L. 1981, *J. Comput. Phys.* 43, 357
- Ryu, D., Jones, T. W., & Frank, A. 1995, *ApJ*, 452, 785
- Sugimoto, K., Hanawa, T., & Fukuda, N. 2004, *ApJ*, 609, 810
- Trottenberg, U., Oosterlee, C. W., & Schüller, A. 2001, *Multigrid* (Academic Press)
- Truelove, J. K., Klein, R. I., McKee, C. F., Holliman, J. H., II, Howell, L. H., & Greenough, J. A. 1997, *ApJL*, 489, L179
- Truelove, J. K., Klein, R. I., McKee, C. F., Holliman, J. H., Howell, L. H., Greenough, J. A., & Woods, D. T. 1998, *ApJ*, 495, 821
- Tóth, G. 2000, *Journal of Computational Physics*, 161, 605
- Woodward, P., & Colella, P. 1984, *Journal of Computational Physics*, 54, 115
- Ziegler, U. 2005, *A&A*, 435, 385

